

Semi-automatic 3D morphological reconstruction of neurons with densely branching morphology: application to retinal AII amacrine cells imaged with multi-photon excitation microscopy

(Research article)

Bas-Jan Zandt^{1,3}, Are Losnegård^{1,4}, Erlend Hodneland^{1,5}, Margaret Lin Veruki¹, Arvid Lundervold^{1,2} and Espen Hartveit¹

¹Department of Biomedicine, University of Bergen, Bergen, Norway

²Department of Radiology, Haukeland University Hospital, Bergen, Norway

³Current affiliation: Blue Brain Project, École polytechnique fédérale de Lausanne (EPFL), Geneva, Switzerland

⁴Current affiliations: Department of Radiology, Haukeland University Hospital, Bergen, Norway; Department of Clinical Medicine, University of Bergen, Bergen, Norway

⁵Current affiliation: Christian Michelsen Research, Bergen, Norway

Corresponding author: Espen Hartveit, University of Bergen, Department of Biomedicine, Jonas Lies vei 91, N-5009 Bergen, Norway.

espen.hartveit@biomed.uib.no

Abbreviated title: Automatic reconstruction of densely branching neurons

Number of pages: 47

Number of figures: 11

Number of tables: 2

Number of words: Abstract 250, Introduction 850, Discussion 2306

Keywords: Adaptive thresholding; Computational neuroanatomy; Fast Marching; Morphology; Neuronal reconstruction; Two-photon microscopy; 3D microscopy

Abstract

Background: Accurate reconstruction of the morphology of single neurons is important for morphometric studies and for developing compartmental models. However, manual morphological reconstruction can be extremely time-consuming and error-prone and algorithms for automatic reconstruction can be challenged when applied to neurons with a high density of extensively branching processes.

New method: We present a procedure for semi-automatic reconstruction specifically adapted for densely branching neurons such as the AII amacrine cell found in mammalian retinas. We used whole cell recording to fill AII amacrine cells in rat retinal slices with fluorescent dyes and acquired digital image stacks with multi-photon excitation microscopy. Our reconstruction algorithm combines elements of existing procedures, with segmentation based on adaptive thresholding and reconstruction based on a minimal spanning tree. We improved this workflow with an algorithm that reconnects neuron segments that are disconnected after adaptive thresholding, using paths extracted from the image stacks with the Fast Marching method.

Results: By reducing the likelihood that disconnected segments were incorrectly connected to neighboring segments, our procedure generated excellent morphological reconstructions of AII amacrine cells.

Comparison with existing methods: Reconstructing an AII amacrine cell required about 2 hrs computing time, compared to 2-4 days for manual reconstruction. To evaluate the performance of our method relative to manual reconstruction, we performed detailed analysis using a measure of tree structure similarity (DIADEM score), the degree of projection area overlap (Dice coefficient), and branch statistics.

Conclusions: We expect our procedure to be generally useful for morphological reconstruction of neurons filled with fluorescent dyes.

1. Introduction

Neurons are the fundamental building blocks of nervous systems, and the visualization, characterization and quantitative description of the morphology of single neurons are essential to understanding their structure-function relationships (for review, see Cuntz et al., 2014). Visualization of neuronal morphology can be performed with a multitude of different experimental methods, each with strengths and limitations, but for quantitative studies, digital reconstruction of the three-dimensional (3D) morphology is an essential step (Jaeger, 2001; Jacobs et al., 2010; Evers and Duch, 2014). Such reconstructions have been crucial both for quantitative, morphometric analysis as well as for compartmental modeling of neuronal computation and signal processing (reviewed by Jaeger, 2001; Parekh and Ascoli, 2013). For the last 30 years or so, morphological reconstruction of single neuron morphology has meant manual reconstruction using computer-aided neuronal tracing software and light microscopic imaging (Glaser and Glaser, 1990; Turner et al., 1991; Meijering, 2010; Parekh & Ascoli, 2013). Light microscopic imaging is either done simultaneously with the reconstruction or is used to acquire a digital image stack that is subsequently used for the reconstruction. However, such manual reconstructions can be extremely time-consuming and can suffer from suboptimal accuracy. Accordingly, it becomes a challenge to generate high-quality morphological reconstructions of large numbers of neurons, e.g. to study morphological variation within and between different types of neurons and to study the organization of large, heterogeneous neural networks at cellular and subcellular resolution (e.g. Schneider et al., 2014; Zandt et al., 2016).

The difficulties and challenges of manual, computer-aided morphological reconstructions of single neurons have motivated a number of efforts aimed at automating digital morphological reconstruction (for recent reviews, see Donohue and Ascoli, 2011; Acciai et al., 2016). An additional motivation for such efforts has been the desire to make the process of reconstruction both less subjective and less prone to errors resulting from misinterpretations and operator fatigue. Some recently published methods have adopted algorithms and procedures based on well-established

principles of image processing, whereas others have developed new algorithms directly aimed at tackling challenges that are specifically linked to reconstructing neuronal morphologies (for examples, see Evers et al., 2005; Santamaría-Pang et al., 2007, 2015; Losavio et al., 2008; Rodriguez et al., 2009; Cuntz et al., 2010, 2011; Chothani et al., 2011; Peng et al., 2011a; Türetken et al., 2011; Zhao et al., 2011; Myatt et al., 2012; Basu et al., 2013; Xiao and Peng, 2013; Feng et al., 2014). To foster development of new methods and algorithms, several initiatives have been launched, e.g. the DIADEM (Digital Reconstruction of Axonal and Dendritic Morphology; <http://diademchallenge.org>) challenge involving an international contest with monetary rewards (Ascoli et al., 2009; Gillette et al., 2011b). The DIADEM challenge has resulted in several published methods (see Gillette et al., 2011b) and a useful evaluation framework for comparing reconstructions to the corresponding manual "gold standard" reconstructions (Gillette et al., 2011a), as well as freely available data sets with light microscopic images of neuronal morphology (Brown et al., 2011). More recently, the BigNeuron project (<http://bigneuron.org>) was launched to establish an open platform and framework where automatic reconstruction methods can be ported to a common software platform, allowing them to be validated against large neuron datasets (Peng et al., 2015). In addition to such collaborative community projects, there are also important commercial developments with the goal of developing both semi-automated and fully automated methods for single neuron reconstruction (e.g. Neurolucida 360 from MBF Bioscience and Imaris FilamentTracer from Bitplane).

A specific difficulty for developing robust algorithms for morphological reconstruction is that the performance of different algorithms may be challenged by specific neuron morphologies. The presence of multiple branching processes is common to almost all neurons, but the variability between different types of neurons is enormous, especially with respect to the dendritic processes (Ramón y Cajal 1909, 1911). In the course of a project where we performed manual, computer-aided morphological reconstructions of rat retinal AII amacrine cells that had been filled with fluorescent dyes intracellularly and imaged with multi-photon excitation (MPE)

microscopy (Zandt et al., 2016), we became increasingly interested in supplementing our reconstructions with semi-automatic or fully automatic reconstructions. All amacrine cells are small, narrow-field amacrine cells and found in all mammalian retinas. Whereas they are small cells, their processes branch extensively and the density, measured as the length/volume ratio, is very high (Zandt et al., 2016). Because we experienced limited success with both commercial and freely available (academic) software for automatic tracing, we have developed a method where we combined elements of other reconstruction procedures, with the goal of performing accurate semi-automatic reconstructions of these densely branching neurons. Briefly, we developed a reconstruction algorithm based on the TREES toolbox approach (Cuntz et al., 2010, 2011) and extended this with an algorithm for connecting disconnected neuron segments with image-extracted paths using the Fast Marching method (Sethian, 1996). To evaluate our method, we compared the results with those obtained by manual, computer-aided reconstructions using a measure of tree structure similarity (as implemented in the DIADEM metric; Gillette et al., 2011a), by calculating the degree of projection area overlap expressed by the Dice coefficient (Dice, 1945), and by analyzing the branch statistics.

2. Materials and methods

In this section we describe the materials and methods for cell preparation and MPE microscopic imaging, initial image enhancement by deconvolution and the removal of both recording pipette and extraneous fluorescence, with the latter caused by leakage of dye from the pipette and binding to dead cells and debris. We then provide details about the image segmentation, the morphological reconstruction process, and the conversion of the binary segmentations into a representation suitable for surface rendering and visual inspection. Finally, we describe the evaluation procedure used to compare the results obtained by automatic and manual segmentation. Although our procedure is semi-automatic, as opposed to fully automatic, we will henceforth refer to

it as automatic for simplicity. Unless otherwise noted, digital processing was performed with MATLAB (R2015b, MathWorks, Natick, MA, USA).

2.1. Retinal slice preparation

General aspects of the methods have previously been described in detail (Hartveit, 1996; Zandt et al., 2016). Albino rats (female; 4 - 7 weeks postnatal) were deeply anaesthetized with isoflurane in oxygen and killed by cervical dislocation (procedure approved under the surveillance of the Norwegian Animal Research Authority). Retinal slices (100 - 200 μm thick) were visualized using a custom-modified "Movable Objective Microscope" (MOM; Sutter Instrument, Novato, CA, USA) with a $\times 20$ water immersion objective (XLUMPLFL; 0.95 NA; Olympus) and infrared Dodt gradient contrast videomicroscopy (Luigs & Neumann, Ratingen, Germany; Dodt et al. 1998). Recordings were carried out at room temperature (22 - 25 °C).

2.2. Solutions and electrophysiological recording

The extracellular perfusing solution was continuously bubbled with 95% O_2 - 5% CO_2 and had the following composition (in mM): 125 NaCl, 25 NaHCO_3 , 2.5 KCl, 2.5 CaCl_2 , 1 MgCl_2 , and 10 glucose, pH 7.4. The recording pipettes were filled with an intracellular solution of the following composition (in mM): 125 K-gluconate, 5 KCl, 8 NaCl, 0.2 EGTA, 10 Hepes, 4 MgATP, and 0.4 Na_3GTP (pH was adjusted to 7.3 with KOH). The pipette solution also contained Alexa Fluor 594 hydrazide (40 - 60 μM), as a sodium salt (Invitrogen / Molecular Probes).

Patch pipettes were pulled from thick-walled borosilicate glass (outer diameter, 1.5 mm; inner diameter, 0.86 mm; BF150-86-10; Sutter Instrument) and the open tip resistance was 7 - 12 $\text{M}\Omega$ when filled with the intracellular solution. Whole cell voltage clamp recordings were performed with an EPC10-triple amplifier controlled by PatchMaster software (HEKA Elektronik, Lambrecht/Pfalz, Germany). During image acquisition, cells were voltage clamped at a holding potential of -60 mV (corrected for the liquid junction potential).

2.3. MPE microscopy and image acquisition

MPE microscopy was performed as described in detail previously (Zandt et al., 2016). Briefly, fluorescence from neurons filled with Alexa 594 was imaged with the MOM equipped with a mode-locked Ti:sapphire laser (Mai Tai DeepSee; SpectraPhysics, Irvine, CA, USA) tuned to 810 nm. Scanning was performed by galvanometric scanners (XY, Cambridge Technology; Cambridge, MA, USA) with 3 mm mirrors. Fluorescence was detected by multialkali photomultiplier tubes (R6357, Hamamatsu Corp.; Bridgewater, NJ, USA) and the analog signals were digitized by an acquisition board (NI-6110E, National Instruments, Austin, TX, USA). The intensity of the laser light was attenuated and controlled by an electro-optic modulator (350-80LA with BK option; ConOptics, Danbury, CT, USA) driven by a 302RM amplifier (ConOptics). An image stack was acquired as a series of optical slices (each slice 1024×1024 pixels; XY pixel size from ~ 64 to ~ 83 nm) collected at a focal plane interval (Z) of $0.4\text{ }\mu\text{m}$, satisfying Nyquist rate sampling (for details, see Zandt et al., 2016). At each focal plane, two images were averaged on-line to improve the signal-to-noise ratio. For each image stack, we acquired two channels, one for fluorescence light and one for IR light (laser scanning gradient contrast imaging; see Zandt et al., 2016). MPE microscopy and image acquisition were controlled by ScanImage software (version 3.8; Pologruto et al., 2003) running under MATLAB.

2.4. Deconvolution

The multi-channel image stacks were de-interleaved based on acquisition channels (using IGOR Pro, version 6, 64-bit, WaveMetrics, Lake Oswego, OR, USA) and saved as individual files (one per channel). Huygens Essential (version 4 64-bit; Scientific Volume Imaging, Hilversum, The Netherlands) was used to remove noise and reassign out-of-focus light with a theoretically calculated point spread function (PSF), using the Classic Maximum Likelihood Estimation (CMLE) deconvolution method. In addition, the Object Stabilizer module was used to align images along the Z-axis to compensate

for drift and mechanical instabilities. Processed image stacks were saved in 16-bit TIFF format, utilizing the whole dynamic range and used without further modifications for manual reconstruction. For automatic reconstruction, the files were converted in Fiji (Schindelin et al., 2012) to the NRRD format for easier handling in MATLAB. For an individual neuron, the same image stack was used for both the manual and the automated segmentations.

2.5. Manual 3D morphological reconstruction

Morphological reconstruction of the fluorescently labeled cells was done manually with computer-aided neuronal tracing software (Neurolucida; version 11 64-bit; MBF Bioscience, Williston, VT, USA; Glaser & Glaser, 1990) by one of the authors (BJZ). 3D reconstruction of the soma was performed by tracing it with multiple contours at a series of focal planes corresponding to different slices of the image stack. As the diameter of the thinnest processes of AII amacrine cells cannot be adequately resolved by light microscopy, we set the minimum diameter of any process to $0.23\text{ }\mu\text{m}$ (Zandt et al., 2016). To reduce the abrupt steps in the Z-direction that often are generated during manual reconstruction, we smoothed the reconstructed trees with the *smooth_tree* function in the TREES toolbox (Cuntz et al., 2011) (using default parameters, effective for the Z-coordinates).

2.6. Image preprocessing

Before the automated cell segmentation could be initiated, it was necessary to remove the image of the recording pipette used to fill the cell with fluorescent dye. During this step it was also advantageous to remove any extraneous fluorescence due to leakage from the pipette. If such false signals are not removed, they will be treated by the segmentation algorithm as if they belong to the cell, as their intensity can be considerably above background levels (see section 2.7 below). We found that the most expeditious way to remove both the pipette and such false signals was to manually circumscribe the area containing the soma and the dendritic tree in a frontal (XY)

maximum-intensity projection (MIP) of the image stack, using the *getline* function in MATLAB. This function allows the user to use a computer mouse to click on the MIP to determine the points of a polygon that will demarcate the region of interest. The 2D contour was extruded to a 3D volume of interest and image intensity values for voxels outside this volume were set to zero. At the same time, this procedure also demarcated the border between the soma and pipette. Before thresholding was used to perform an initial intensity segmentation of a cell, the image stack was smoothed by applying a coherence enhancing diffusion filter (Weickert, 1997).

2.7. Initial intensity segmentation of the cell

To segment the geometrically complex and intensity-varying dendritic tree, we applied adaptive thresholding. We used adaptive filter size $r = [2.5, 2.5, 5]$ (μm). To prevent noise from being segmented, the adaptive threshold was increased by a constant equal to 5% of the maximum image intensity (i.e., the background addition for the adaptive thresholding routine was set to 0.05, cf. Hodneland et al., 2013). In thick structures with sizes comparable to the adaptive filter size, i.e. the soma and primary dendrite, indentations or holes would sometimes occur after adaptive thresholding. Therefore, a second segmentation was performed by applying a global threshold (heuristically set to 11% of the maximum image intensity), followed by morphological operations to identify the largest connected component. This resulted in a segmentation containing the soma and neck of the primary (apical) dendrite, in addition to the segmentation obtained from adaptive thresholding. The union of these two segmentations was constructed for further use. This procedure was followed by removal of components smaller than 20 voxels (which were regarded as noise). The next step was to connect the disconnected components generated by the initial segmentation.

2.8. Fast Marching arrival times

The Fast Marching method is a versatile path extraction technique (Sethian, 1996) and was used to compute the optimal paths to connect disconnected segments. It approximates the solution of the Eikonal equation:

$$|\nabla T|F = 1, \quad (1)$$

where T is the so-called arrival time and F is the speed of a moving front, with the arrival time gradient and the front speed being inversely proportional.

The Fast Marching arrival times were computed for all voxels in the stack, using a point in the soma as a starting point and using the original (preprocessed) image intensity as the speed function. The choice of the speed function was motivated by the fact that the thinnest processes, which we were not able to segment using thresholding, were still brighter than the average background level. Consequently, the marching time between two segments with a thin process running directly between them (in the original image) will be lower than the marching time between two segments having only background voxels between them (i.e., intensity close to zero in the original image stacks).

2.9. Connecting disconnected segments by the Fast Marching method

Segments were merged by back tracing the Fast Marching arrival time map T from each segment to the soma. To automatically select a point roughly in the center of the soma, our procedure calculated the center of mass (XY position) of the 100 brightest pixels in an additive Z-projection of the preprocessed stack. The Z-coordinate was determined by finding the voxel at this XY position with the largest distance to the background in the thresholded stack, using a distance transform. For each segment, the voxel with the lowest arrival time mapped to it was taken as the starting point. To prevent the back tracing from getting stuck in regions with zero intensity, the speed function was set to a minimum of 1e-8.

The Fast Marching arrival time map T increases monotonically from the soma center point, and back tracing from the disconnected segments can be performed using the steepest descent method:

$$x_{n+1} = x_n - h \nabla T(x), \quad (2)$$

where $n = 0, 1, 2, \dots; x = (x, y, z); T(x_0) \geq T(x_1) \geq T(x_2) \geq \dots$, and h is the step length. For a constant speed function F , the back tracing would give straight lines between start and end points. However, for non-constant F , the back tracing pathway is attracted to voxels with high intensity values, i.e. where F is high. Binary representations of the cells were created by joining the voxels traversed by the connection paths and the segments from the initial intensity segmentation of the cells (as described in section 2.7).

2.10. Tree representation

The binary cell representation generated by the automated segmentation was transformed to a tree representation following the definitions of the SWC-format, a simple tabular text format that lists a set of (X, Y, Z) positions and associated tubular radii (Cannon et al., 1998). Skeletonization of the segmented volume, i.e., thinning the segmented volume by erosion of the surface (Lee et al., 1994), was performed by the *Skeletonize3D* function in Fiji, called automatically from within MATLAB. Prior to skeletonization, all slices within the segmented volume were smoothed (3×3 pixel mean filter) and binarized by the *Smooth* and *Make Binary* functions in Fiji. The coordinates of the voxels in this skeleton were then used to generate a minimum spanning tree (MST; Prim, 1957) using the TREES toolbox (Cuntz et al., 2010, 2011). An MST simultaneously optimizes the total branch length and the total path length to soma for all points. The relative weight between the wiring cost and the path length cost is controlled by a so-called balancing factor. Since the resulting points in the skeleton are closely spaced on the dendrites, there is little ambiguity in how they should be connected. Considering the optimized total path length to soma is therefore of little advantage. Accordingly, we used a small balancing factor of 0.01, essentially drawing the shortest possible connections between points.

2.11. Determination of branch diameter

In image stacks acquired by light microscopy, the axial optical resolution (in the Z-direction) is inherently lower than the lateral optical resolution (in the X- and Y-directions) (reviewed by Murphy and Davidson, 2013). The cross-sections of the branches of the automatically segmented volume are therefore elliptical, i.e. much thicker in the Z-direction. We corrected for this by a process of "tubularization", whereby the diameter associated with each reconstruction point (each voxel in the tree structure after skeletonization) was calculated as twice the distance from the point to the closest border of the segmented volume. This diameter is equal to the diameter of the largest sphere, centered at the reconstruction point, that could be fitted into the segmented volume. These diameters were obtained by calculating the Euclidean distance transform of the segmented image (using MATLAB's *bwdistsc* function) (Paglieroni et al., 1992; Maurer et al., 2003; Mishchenko, 2015). A minimum diameter of 0.23 μm was enforced (see section 2.5 above).

2.12. Corrections

First, possible false branch endings introduced in the neuronal tree during skeletonization were removed using the *clean_tree* routine in the TREES toolbox (Cuntz et al., 2010, 2011). This routine removes branches shorter than a specified length parameter (termed *radius*) and branch endings within a specified distance parameter (*radius*) from other branch endings. Based on empirical testing, we set the *radius* parameter to 0.2 μm . Second, when the skeletonization algorithm attempted to represent the soma volume, it typically generated a number of false branches in the region inside and close to the outside of the soma. We investigated the possibility to automatically remove the spurious branches by the following procedure. First, we determined the approximate center of the soma (see section 2.9 above) and an ellipsoid was fitted inside the segmented volume. Then, we removed all reconstruction points inside this ellipsoid. To reliably remove all spurious branches, however, the ellipsoid lengths had to be slightly enlarged (by a factor of ~1.3). Unfortunately, this also removed parts of the reconstructed apical dendrite and smaller branches emanating

directly from the soma. Therefore, instead of a fully automatic method, we chose a semi-automatic approach with manual delineation of the region where the spurious branches occurred. In our procedure, the user is prompted to draw the outline of this region (using Matlab's *getline* function), first in a front view projection (XY) and then in a side view projection (YZ). In these views, the generated skeleton was overlaid on a maximum intensity projection of the pre-processed image stack. Points were removed if both their XY-coordinates and their YZ-coordinates were inside the corresponding outlines. We found this much more efficient than to manually remove any spurious branches that were left over in cells where automatic removal was only partially successful.

Whereas both manual and automatic reconstructions can suffer from discrete steps along the Z-dimension, we found that the automatic reconstructions also suffered from a similar phenomenon along the X- and Y-dimensions, because of the large number of reconstruction points per unit branch length. Because this problem artificially increased the branch length, we spatially filtered the automatic reconstructions using the *smooth_tree* function in the TREES toolbox (Cuntz et al., 2011) (using default parameters).

2.13. Volume reconstruction

To enable assessment of overlap between the manual and automated segmentations, both tree representations were converted to binary masks (with the same voxel dimensions as the original stacks). For the manual cell reconstructions, we converted the corresponding files from ASC format (Neurolucida) to SWC format using NL Morphology Converter (<http://www.neuronland.org>). The tree-to-volume transformation was then done by adding spheres along the (X, Y, Z) points listed in the SWC file. These points were too sparse to achieve a smooth surface, so the trees were first upsampled to have 1 voxel distance between reconstruction points (using the TREES toolbox). In this way we obtained binary masks that could be used to calculate Dice coefficients and generate isosurface renderings.

2.14. Generating the soma contour

As a final step, a representation of the soma was added to the SWC file. After segmentation of the cell, our procedure generated a single contour to represent the soma. The procedure automatically traced the soma outline in the individual slices of the segmented image stack (obtained from the procedure described in section 2.7) and then selected the one with the maximum area. First, it found a point (XY-coordinate) approximately in the center of the soma by calculating the center of mass of the 100 brightest voxels in an additive intensity projection of the whole image stack. Then, it processed each image slice of the segmented image stack individually to find the contour of the soma in that slice. The contours in the image were calculated and the one enclosing the center point was selected. The radius of this contour as a function of angle was calculated with the initial center point as origin (3.6° resolution). In the next step, process-like extensions were eliminated from the soma contour by removing peaks smaller than an angle $\Delta\theta$ in an angular plot of the radii (using MATLAB's *ordfilt2* function). An optimal $\Delta\theta$ was heuristically determined as 36 degrees. To counteract the possibility of a sub-optimal initial determination of the soma center, a new center point was then calculated as the center of mass of the contour, and the procedure was iterated. The iteration typically converged in three steps, so for good measure we performed 10 iterations for each individual image slice. After processing all slices in the image stack, the procedure calculated the area of the contour in each slice and plotted the area as a function of the Z position in the stack. The contour in the center of the soma, typically the contour with the largest area, was then selected by finding the peak of this curve, after smoothing (2nd order Savitzky-Golay filter with window length set to $8 \mu\text{m}$, equal to the typical diameter of the soma).

2.15. MATLAB implementation

The algorithms for segmentation of the cell from the background, the Fast Marching method and the tree generation were all implemented in MATLAB R2015b, partly by

using functions from the TREES toolbox (v 1.15; Cuntz et al., 2010, 2011), the Accurate Fast Marching toolbox (Kroon, 2009) and the CellSegm toolbox (Hodneland et al., 2013).

2.16. Performance evaluation

Manual and automated segmentations were compared using the metric developed for the DIADEM challenge (Gillette et al., 2011a), the Dice Coefficient (Dice, 1945), and analysis of branch statistics (using functions from the TREES toolbox; Cuntz et al., 2010, 2011). The DIADEM metric score compares two trees represented in the SWC format (Gillette et al., 2011a). The core of the metric compares the nodes in the trees with respect to spatial position and global topology. Since perfect spatial correspondence is rarely obtained, the metric includes parameters that allow the user to set distance thresholds for the matching. The parameters x and z are the Euclidean distances defining the neighborhood in the XY-plane and along the Z-direction, respectively, in which a node is searched for, and set the maximum distances between a gold standard node (i.e., a node obtained from the manual segmentation) and an acceptable node in the test segmentation (i.e., a node obtained from the automated segmentation). In addition, the ancestor nodes of this pair of nodes are compared. To allow for small deviations when comparing the node-to-ancestor-node path length in the gold standard with the corresponding path length in the test segmentation, the parameters $xyPathThresh$ and $zPathThresh$ specify the allowed relative path length deviations in the XY- and Z- directions, respectively. In order to obtain an accurate score for the quality of the reconstructions, we visualized and manually inspected the missed and extra branches in our automatic reconstruction as reported by the DIADEM algorithm. We manually adjusted the parameters for node matching distances and path length tolerances, such that we approximately observed the fewest false positives and false negatives (for accuracy), as well as approximately equal numbers of false positives and false negatives (for fairness). The optimal setting was determined as $x = 3 \mu\text{m}$, $z = 3 \mu\text{m}$, $xyPathThresh = 0.2$ and $zPathThresh = 0.2$.

The Dice coefficient (DC) is a measure of set similarity and can be used to assess the overlap between two segmented objects. If A and B are two objects, then

$$DC = \frac{2|A \cap B|}{|A| + |B|}. \quad (3)$$

To determine a Dice coefficient, we compared the areas of the frontal (XY) maximum intensity projection. Volumes were not compared because the size of the voxels in the Z-direction is approximately equal to the typical branch diameter ($0.4 \mu\text{m}$), such that the Dice coefficient would only reflect the fraction of branches displaced by one voxel in the automated reconstruction relative to the manual reconstruction.

To allow a comparison with other reconstruction algorithms, we also reconstructed the set of nine olfactory projection fibers used in the DIADEM competition (Brown et al., 2011). For this set we changed the adaptive filter size to $r = [10, 10, 20]$ (XY-pixel sizes), the cleaning *radius* parameter to 2 (XY-pixel sizes), and manually set the roots of the trees to the positions stated in the DIADEM data set. A DIADEM score for the reconstructions of the olfactory projection fiber data set was computed with the parameters as used in the DIADEM competition ($x = 3.94$ pixels, $z = 5$ images, $xyPathThresh = 0.08$ and $zPathThresh = 0.2$).

Data are presented as the mean \pm SD.

Figure 1 near here

3. Results

3.1. Semi-automated reconstruction pipeline

Our semi-automated reconstruction pipeline is summarized as a flowchart in Fig. 1. The pipeline consists of four major parts which we have termed preprocessing (including deconvolution), segmentation, skeletonization and tubularization, and postprocessing. In the following, we will illustrate examples of the results obtained at the various stages along this workflow. For All amacrine cells, we are able to acquire image stacks at the resolution required for Nyquist sampling as single volumes. For larger neurons that require acquisition of multiple tiled stacks, an additional step with

registration of a number of such stacks would be necessary to generate a single supervolume (e.g. Losavio et al., 2008).

Figure 2 near here

3.2. Image preprocessing and deconvolution

Deconvolution is a powerful image processing technique to increase the signal-to-noise ratio and decrease the axial and lateral blurring (van der Voort and Strasters, 1995). As described in detail for a previous study from our laboratory (Zandt et al., 2016), the deconvolution software requires user input of several microscope and imaging parameters and an additional parameter that controls the sharpness of the final image. Fig. 2A shows a maximum intensity projection (XY plane) of the cell before deconvolution and Fig. 2B shows the same after deconvolution (using Huygens Essential). After the deconvolution, the user is instructed to denote a region of interest (ROI) to circumscribe the relevant structures belonging to the cell, excluding the pipette and any contaminating extraneous fluorescence due to leakage from the pipette used to fill the cell with dye. Examples of areas of such extraneous fluorescence are illustrated by the areas marked by dotted lines in Fig. 2B. Whereas the ROI needs to precisely follow the transition between the cell body and the pipette tip, the dendritic tree can be more coarsely outlined (Fig. 2C).

Figure 3 near here

3.3. Intensity segmentation

To prevent noise from being segmented during adaptive thresholding, we increased the threshold value by a constant that by default was set equal to 5% of the maximum image intensity. In general, the result of the segmentation was fairly insensitive to the specific value selected for background addition. However, for three of our image stacks (3/10 cells), the highest intensity in the image (located at the soma) was considerably higher than the intensity throughout the rest of the cells. For these image stacks, the background addition was lowered to 1 or 2%. Segmented components with

fewer than a specified number of voxels were considered to be noise and were removed. For the AII amacrine cells, we obtained reasonable results by setting this criterion to 20 voxels. However, for other image stacks and cell types, the optimal value may differ and must be determined empirically.

The thresholding generated a binary representation of the cell and typically resulted in cells that consisted of multiple disconnected components, as illustrated by an example in Fig. 3A. In the next step, these disconnected components were connected by the Fast Marching method that involved calculating a map of the arrival times from the soma center (see Materials and methods). Fig. 3B, C shows an example of how this procedure connected the originally disconnected components to the rest of the cell by marking the paths from all the originally disconnected components ($n = 62$ components; Fig. 3A) to the soma. In the final result, single voxel-thick paths connected all components into a single volume (Fig. 3D).

Figure 4 near here

3.4. Skeletonization and tubularization

In the next steps of the algorithm, the binary representation generated by the segmentation was transformed to a tree representation. After smoothing the segmented volume, skeletonization was performed by thinning the segmented volume using voxel erosion. A representative result of the skeletonization procedure is illustrated in Fig. 4A. A weakness of the skeletonization procedure is that it typically generated a multitude of false branches inside and around the soma (Fig. 4B). The most efficient way we have found to remove such false branches, involves prompting the user to demarcate a ROI around the soma, both in the front (XY; Fig. 4B, top) and the side (YZ; Fig. 4B, bottom) view. The coordinates of the voxels in the skeleton were used to generate an MST, using algorithms of the TREES toolbox (Cuntz et al., 2010, 2011). The nodes of false branches inside the corresponding volume were then removed (Fig. 4C). In addition, small branches were cleaned from the tree structure by the *clean_tree* function of the TREES toolbox. In the final step of this part, the tree structure was

converted by a process of "tubularization" to a structure where each reconstruction point received an associated diameter (Fig. 4D).

Figure 5 near here

The procedure adopted for tubularization is necessitated by the fact that for image stacks acquired by light microscopic imaging, the optical resolution is inherently lower in the axial direction than in the lateral direction, meaning that imaging a structure that is perfectly round in cross section will result in a structure that has an elliptical cross section, with a larger diameter in the axial direction than in the lateral direction (Fig. 4A). For each reconstruction point, the diameter of the corresponding tubular process was set as the diameter of the largest sphere (centered at the reconstruction point) that could be fitted into the segmented volume. This is illustrated in more detail in Fig. 5A, B that compares the result from the segmentation (red lines) with the result after tubularization (yellow lines). For the projection in the XY-plane (Fig. 5A), there was little difference, as is expected, but for the projection in the YZ plane (Fig. 5B) it can readily be seen that the tubularization effectively corrected for the lower axial resolution. For comparison, the resulting tubularization was also overlaid on the manual, computer-aided reconstruction (Fig. 5C, D). Such reconstructions are performed exclusively by manual delineation of processes and their diameters when the image stack is displayed as slices viewed in the XY plane, effectively forcing the diameters obtained for this plane to be used as the diameters in the axial direction. As illustrated in Fig. 5C, D, the results of the tubularization were in very good correspondence with the manual reconstruction, both as viewed in the XY plane and in the YZ plane.

Fig. 6 near here

3.5. Generating the soma contour

For small cells, such as AI amacrine, the soma represents a significant fraction of the total area of the cell, and precise reconstruction is important. In general, a soma can be represented either by a single contour, multiple contours, multiple cylinders, a "three-

"point soma", or a single sphere (<http://neuromorpho.org/SomaFormat.html>). Because light microscopic imaging artificially elongates the soma in the axial direction (Fig. 4A), we chose a single soma contour representation (defined in the XY plane). Most analysis and simulation programs (e.g. NEURON, L-measure) correctly handle files with single soma contours by assuming that the soma has a primary axis in the XY-plane and is rotationally symmetric.

The first step in our procedure was to set a point (XY) approximately in the center of the soma (see section 2.14), indicated by the white cross in the example illustrated in Fig. 6A. Then, the contour of the object containing this point was determined for each image in the segmented image stack (Fig. 6A) and the radii of each contour were plotted as a function of angle (Fig. 6B). These contours typically displayed process-like extensions (see examples in Fig. 6A and the corresponding radii in Fig. 6B) and these were eliminated by removing peaks in the radius versus angle plot (Fig. 6B). A new center point was then calculated as the center of mass of the corrected contour. The procedure was re-iterated 10 times to ensure convergence. An example of the end result is illustrated in Fig. 6C. When all the slices in the image stack had been processed in this way, the procedure calculated the area of the soma contour in each slice and plotted the area as a function of position in the stack (Fig. 6D). After smoothing the curve, the central contour at the peak was selected to represent the soma (Fig. 6D).

Fig. 7 near here

3.6. Qualitative comparison of automatic and manual reconstructions

For visual comparison of the overall similarity between automatic and manual reconstructions, we used the tree representations (in the SWC format) generated after cleaning and removal of spurious nodes inside and around the soma (see section 2.12). Visual inspection and comparison of the reconstructions confirmed that overall, the automatic reconstructions accurately reproduced the manual reconstructions. An example of this is illustrated by the AII amacrine cell displayed in Fig. 7. The cell

branched extensively within a relatively small volume, as is typical for these cells (cf. Zandt et al., 2016). The tree structures generated by the automatic and manual reconstructions are shown in Fig. 7A and 7B, respectively, and suggest a high correspondence between the two methods. An overlay of the two trees verifies the correspondence (Fig. 7C). The DIADEM algorithm detects mismatches both as spurious and missed nodes (branch points). Spurious nodes (marked by x and X in Fig. 7) are nodes in the automatic reconstruction that were not matched by nodes in the manual reconstruction. Missed nodes (marked by o and O in Fig. 7) are nodes in the manual reconstruction that were not matched by nodes in the automatic reconstruction. The small markers (x, o) denote mismatches located at branch endings, while the large markers (X, O) denote mismatches of (centripetally) higher-order branch points. It is clear from Fig. 7 that most mismatches correspond to spurious and missed branch endings, while the main structure is accurately obtained with few errors (five spurious and two missed higher-order branch points for the example shown in Fig. 7).

Fig. 8 near here

We also judged the degree of area overlap of the automatic and manual reconstructions. Fig. 8 shows projections of isosurface renderings (using the radii along the tree) of the same cell illustrated in Fig. 7, both for automatic (Fig. 8A) and manual (Fig. 8B) reconstructions and both for front (XY; top row) and side (YZ; bottom row) views. The degree of overlap appears very high and this was confirmed when the two projections were overlaid (Fig. 8C; top and bottom). From inspection of the front and side views, it can be seen that our method produced similar diameters for both arboreal and lobular dendrites, as well as for the dendritic varicosities which are characteristic for AII amacrine cells.

Fig. 9 near here

For a more detailed comparison of manual and automatic reconstructions, including details of missed and spurious branches, we inspected multiple regions with side-by-side comparisons of maximum intensity projections of the image stack overlaid

with the reconstructions. For the AII amacrine cell illustrated in Fig. 9A, we show examples of four different subregions that include the soma (Fig. 9B), lobular dendrites and appendages (Fig. 9C), and arboreal dendrites (Fig. 9D, E). The overlays were constructed by rendering the tree representations of the automatic and manual reconstructions as a set of short cylinders (TREES toolbox) displayed on top of the maximum intensity projections of the image stack (Fig. 9B-E; "Automatic", "Manual"). In addition to the overlays, we also show the projection of the volumes of the two reconstructions, including their overlap (Fig. 9B-E; "Projected volume"). Finally, to compare the tree structures we display the branches overlaid (Fig. 9B-E; "Schematic"). Overall, the correspondence between the dendritic trees is quite remarkable (Fig. 9B-E), although at a more granular level there are many examples of how the automatic and manual reconstructions differ from each other. In general, the automatic reconstruction accurately followed the variation of thickness along the dendrites and varicosities (Fig. 9B-E), but the diameters of the automatically reconstructed segments tended to be slightly larger than those of the manually reconstructed. Furthermore, on several occasions the algorithm generated or missed short branches (Fig. 9C-E, see also Fig. 7).

Fig. 9B shows small branches arising from and located close to the soma. Branches in this region can be very difficult to reconstruct (both manually and automatically) due to scattered light originating from the very bright soma. While the rightmost branch in Fig. 9B was correctly reconstructed by the automatic procedure (left panel), the branch extending upwards from the apical dendrite was cut (bottom arrow) and wrongly connected to the soma close to where its distal end should have been. In addition, one valid branch in front of the soma (center arrow) was removed from the automatic reconstruction during the cleaning of spurious branches around the soma. Finally, an additional branch behind the soma was detected (top arrow). Closer inspection of the image stack revealed that this branch was actually correctly detected, but missed during manual reconstruction.

Fig. 9C shows a region with multiple lobular dendrites and lobular appendages close to the soma and illustrates a series of typical errors: a branch tip that was too

short (left arrow), a small branch that was missed (center arrow), and a spot of low fluorescence intensity detected as a small branch by our algorithm (right arrow), but that was considered noise during the manual reconstruction. Fig. 9D shows a region corresponding to the distal part and terminal branches of arboreal dendrites and illustrates two relatively minor errors: missing a small branch (top arrow) and terminating another branch too early (bottom arrow). Fig. 9E shows a more proximal region of the arboreal dendritic tree and illustrates a typical error that can occur in the relatively rare situation where branches cross in the XY plane and are close to each other along the Z axis. In such cases, distal branches are usually connected to the parent branch that has the shortest path to the soma. In the present case, a small branch extends from the branch on the right towards the vertically oriented branch on the left. Just proximal to the crossing of these two processes, the algorithm cut the vertical process (arrow) and incorrectly connected its distal part to the small branch. From the projected volumes (Fig. 8, 9B-E), it can be seen that for most regions of the dendritic tree, the automatic reconstruction overall produced slightly thicker processes than the manual reconstruction.

Table 1 near here

3.7. Quantitative comparison of automatic and manual reconstructions

To quantitatively compare the results of the automatic and manual reconstructions, we used the metric developed for the DIADEM competition (Gillette et al., 2011a), the Dice coefficient (Dice, 1945), and analysis of branch statistics. To use the DIADEM metric for comparison between two tree structures, they need to be represented in the SWC format (Gillette et al., 2011a). The automatic reconstructions were generated in this format by default and the manual reconstructions generated with Neurolucida software were converted to the SWC format by the program NL Morphology Converter. For calculating the DIADEM score, we used files without soma representations. For the 10 AII amacrine cells reconstructed, the average DIADEM metric score was 0.950 ± 0.019 (range 0.920 - 0.972) and Table 1 shows individual scores

for these cells. To use the Dice coefficient for comparison, we measured the areas of the maximum intensity projections in the XY plane (cf. Fig. 7) for each of the manually and automatically reconstructed cells. The average Dice coefficient was 0.857 ± 0.014 (range 0.826 - 0.875) and Table 1 shows individual coefficients for these cells.

Fig. 10 and Table 2 near here

To further assess the degree of similarity between the automatic and manual reconstructions, we analyzed the branch statistics (using functions in the TREES toolbox), including number of branch points (nodes) and endings, branch length, the average diameter, and surface area (for review, see Capowski, 1989). Table 2 shows the distribution of the properties we measured, as well as the ratios between the measurements for automatic and manual reconstructions.

Despite a high degree of overall similarity, we identified three important differences between the automatic and manual reconstructions. First, the automatic reconstructions overall generated a number of spurious, short terminal branches that were missing in the manual reconstructions (see section 3.6 and Fig. 7), increasing the number of branch points and endings by ~50% (Table 2). This can be seen from the distribution of branch segment path lengths illustrated in Fig. 10A, reflecting the larger number of branch segments shorter than $\sim 5 \mu\text{m}$ in the automatic reconstructions. This is not only due to the short length of the additional branches, but is magnified because adding a branch splits the parent branch segment into two shorter segments. If we removed all terminal branch segments shorter than $1 \mu\text{m}$, the distributions were very similar for automatic and manual reconstructions (Fig. 10B).

Second, the automatic reconstructions sometimes contained a few branches generated by connecting to regions with spurious fluorescence (typically 0 - 5 branches, but two reconstructions contained 12 and 20 such branches, respectively). These branches were almost straight and primarily occurred in the dendritic tree closest to the soma where most of the spurious fluorescence was located. An example of a false branch can be seen in the side view (YZ-plane) of Fig. 8A where a one-voxel thick branch extends from the primary dendrite to the right side of the image. This

problem influenced the distribution of the length of processes as a function of the distance from the soma, illustrated by the Sholl analysis (Sholl, 1953) in Fig. 10C. Whereas the distributions were very similar at distances $> 30 \mu\text{m}$ from the soma, the automatic reconstruction generated longer process lengths than the manual reconstruction for distances closer to the soma.

Finally, the branch analysis indicated that the automatic reconstructions overall generated somewhat thicker branches than the manual reconstructions. On average, the diameter (weighted by branch length) was $\sim 27\%$ larger in the automatic reconstructions (Fig. 10D; Table 2). In combination with the larger total branch lengths, this resulted in a surface area that was $\sim 45\%$ larger (Table 2).

In addition to the topological accuracy of the automatic reconstructions, the time required for reconstruction is important. Whereas the processing time obviously will vary according to the size of the image stack and the number of disconnected segments, automatic reconstruction required (in its present implementation) an average of 2 hrs computing time for each preprocessed image stack containing a single AII amacrine cell (100 - 200 slices, each with 1024×1024 pixels) on a 2.6 GHz Intel Core i7 CPU with 16 GB 1600 MHz RAM. This is considerably shorter than the 2 - 4 days required by an expert to manually reconstruct an AII amacrine cell using Neurolucida. During processing of a stack, the most time consuming steps are the adaptive filtering, the calculation of the Fast Marching arrival times map, and the back tracing. The time required for user interaction is minimal (< 5 min) and corresponds to two separate steps in the work flow where the user is requested to denote specific regions of interest (Fig. 1). This estimate assumes that the optimization parameters have been tuned for the specific cell type and image data and that the image stack has already been deconvolved.

Fig. 11 near here

3.8. Performance on the olfactory fiber dataset from the DIADEM competition

As a general validation, we also tested our procedures on the image stacks of the olfactory fiber dataset (Jefferis et al., 2007) from the DIADEM competition (Brown et al., 2011). The automatic reconstructions were compared with gold standard manual reconstructions included in the same datasets. With the standard parameter settings from the competition, the reconstructions generated with our algorithm obtained a DIADEM metric score of 0.870 ± 0.066 . An example of an automatic reconstruction of one of the olfactory projection fibers is illustrated in Fig. 11. It is clear that our algorithm is able to accurately reconstruct the general structure of the neuronal branches (Fig. 11A, D). However, several small branches are missing from the automatic reconstruction and for both the automatic and manual reconstructions there are examples of branch tips that are too short (Fig. 11B, C and E). In contrast to the AII amacrine reconstructions, the considerably smaller stacks of the DIADEM olfactory projection fiber dataset could be reconstructed in approximately three minutes.

4. Discussion

We have designed and tested a user-friendly method for semi-automatic segmentation and reconstruction of densely arborising neurons, using fluorescent images of retinal AII amacrine cells acquired with MPE microscopy. After obtaining an image stack of a fluorescently filled cell, the challenge of morphological reconstruction can be formulated as an object-from-background segmentation problem. Due to limitations of light microscopy to resolve the thinnest neuron processes and the unavoidable presence of noise, images of the tree-shaped neurons are blurred and only partly distinguishable from the background. Our approach employs preprocessing with deconvolution (to enhance the imaged object and sharpen its edges), simple and adaptive intensity thresholding, the Fast Marching method, skeletonization, and calculation of an MST from the skeleton. Our algorithms utilize several existing MATLAB toolboxes, including the TREES toolbox developed by Cuntz et al. (2010, 2011), and combine them in a semi-automatic work flow that requires minimal user

input and takes significantly less time than a manual reconstruction (by a factor of 10 - 20).

4.1. The AII amacrine cell as a test case for morphological reconstruction

In the mammalian retina, AII amacrine cells are important for signal transmission in the inner plexiform layer and serve an important role for both scotopic and photopic signaling (reviewed by Hartveit and Veruki, 2012). They receive glutamatergic synaptic input from both rod bipolar cells and some types of OFF-cone bipolar cells, with the inputs segregated to separate domains of the dendritic tree. Their outputs are conveyed via electrical synapses to ON-cone bipolar cells and via chemical, inhibitory (glycinergic) synapses to OFF-cone bipolar cells and OFF-ganglion cells. In addition, AII amacrines are connected to each other via electrical synapses.

Whereas the challenge posed by the AII amacrine cell in relation to morphological reconstruction stems from the densely branching dendritic tree (for a quantitative analysis, see Zandt et al., 2016), it is important to realize that this is not simply related to the branching pattern as such, but also to the absolute scale (relative to the measurement technique). In other words, had the AII amacrine been a much larger cell, morphological reconstruction (both manual and automatic) would have been considerably easier. In the case of the AII amacrine and other small, densely branching cells, the structure of the dendritic tree brings different processes closely together at a scale where the resolution limit of light microscopy becomes critical.

The extent to which the AII amacrine cell can serve as a general test case for morphological reconstruction procedures is limited by the fact that it is an axon-less interneuron. Despite the recent discovery of an axon initial segment-like process in AII amacrines (Wu et al., 2011; Cembrowski et al., 2012), the AII does not have an axonal tree similar to that found in inhibitory local-circuit neurons like basket cells (e.g. Nörenberg et al., 2010). Accordingly, it remains to be investigated how our procedure will perform when challenged by the addition of densely and extensively branching axonal trees seen in some types of neurons.

For neurons with spiny dendrites, it can be challenging to perform automatic reconstructions because the algorithm has to properly disregard the spines for accurate estimation of the process diameter (cf. Losavio et al., 2008). Although the AII amacrine does not carry spines similar to those seen on e.g. pyramidal neurons in the hippocampus and neocortex, the arboreal dendrites can have spine-like protrusions (e.g. Fig. 2, 9). In no case did we observe that the presence of such structures interfered with automatic reconstruction or the estimation of process diameter. Accordingly, whereas our procedures should be tested on spiny neurons, we do not foresee any major problems for automatic reconstructions of such neurons.

Because the AII amacrine cells are small neurons, we were able to image complete neurons in single stacks even when acquiring at high spatial resolution according to the Nyquist criterion. For larger neurons, it is often necessary to acquire multiple image stacks to obtain complete images, even when the axon terminal is ignored, and before reconstruction it is necessary to register multiple image volumes to make a single, composite image stack. In the regions of overlap between individual image stacks, there will often be transition zones with strong variations in image intensity and this might challenge the performance of automatic reconstruction procedures.

4.2. Proofreading and editing, semi-automatic versus automatic

Although a major motivation for developing procedures for automatic morphological reconstruction is to save time, this cannot be considered in isolation from other criteria. If the time saved during reconstruction is lost during extensive and time-consuming editing of the reconstructed cells, little real progress has been achieved. Given that there will always be some errors in the results of automatic procedures, it was recently emphasized that powerful, real-time visualization tools are important for proofreading and correcting the output of automated algorithms (Peng et al., 2010, 2011b). In the current state of implementation, our procedures do not contain functions for correcting and/or editing such errors. Until such functionality can be developed, the most

convenient way to proofread the results from the automatic reconstructions would be to import them into e.g. Neurolucida (Glaser and Glaser, 1990) or neuTube (Feng et al., 2014), followed by manual editing. The implicit assumption is that even with an additional step of manual error correction, the total reconstruction time will be significantly shorter compared to fully manual reconstructions.

4.3. Limitations and comparison with other methods

A number of different approaches have been taken to develop procedures for automatic neuronal reconstruction (for review, see Meijering, 2010; Santamaría-Pang et al., 2015; Acciai et al., 2016). The more simple and straightforward methods involve thresholding and skeletonization. However, they have several drawbacks compared to methods based on local image features. Most importantly, cells need to have a consistently higher intensity than the background. In addition, such methods do not deal well with branch crossings and they do not scale favorably for images and image stacks that contain multiple neurons. In principle, reconstructing neurons like AII amacrine cells from image stacks acquired with MPE microscopy should be little affected from these drawbacks. In ideal cases, only the cell is filled with fluorescent dye and the background intensity is relatively low. In addition, the problem of branch crossings is relatively low in 3D (cf. Meijering, 2010). Finally, only a single cell is contained within a given image stack. Accordingly, a method that incorporates adaptive thresholding followed by skeletonization should in theory be ideally suited. Nevertheless, there are practical limitations. Branches can suffer from low fluorescence intensity due to their small diameters and/or low levels of fluorescent dye. When the intensity of weakly imaged branches fall below threshold, they will not be segmented correctly by adaptive thresholding routines, typically leading to multiple disconnected segments per cell. For less densely branching cells, such disconnected segments are likely to be reconnected to the correct parent branch when an MST is calculated. For the densely branching AII amacrine cells, however, disconnected segments were often incorrectly connected to neighboring branches. To work around this problem, our

procedure takes advantage of the fact that the image intensities of the voxels between the disconnected segment and the correct branch are usually higher than background. Image intensities are not taken into account when constructing an MST, but we exploited this information by implementing an additional step where a Fast Marching routine was used to reconnect disconnected segments before skeletonization. Although motivated by the specific challenge of reconstructing densely branching AII amacrine cells, we expect this approach to be generally useful for neuronal morphological reconstruction.

In the ideal case, image stacks acquired after filling single neurons with fluorescent dye via pipettes will contain very low background fluorescence. The importance of low background intensity became obvious when we attempted reconstruction of a neuron in an image stack with multiple regions of spurious fluorescent signal (not shown). Such contamination is due to excessive leakage of dye from the pipette used to record from and fill the neuron and tends to be located in the vicinity of the recording site (typically the cell body). Unless the leakage of dye is excessive, distinguishing such regions from neuronal structures rarely proves difficult for an experienced human operator, but the performance of an algorithm simply based on thresholding and skeletonization was very poor. In the result, all segments with intensity above threshold were connected, irrespective of their shape or position in the image. Discarding segmented objects based on size alone is not a robust solution to this problem. This problem may be solved by setting a criterion for discarding segmented components that in addition to size also takes into account the arrival time to the main segmented object (i.e., the cell body). With such an approach, larger regions with spurious fluorescene should be removed if they are further away from the cell and / or are only connected via low intensity voxels. However, when image stacks are strongly dominated by artifacts of this kind, a segmentation method based on local image features is probably preferable over one that is based on thresholding and skeletonization (Meijering, 2010).

In addition to procedures for fully automatic reconstruction of neuronal morphology, different methods for semi-automatic procedures involving variants of "finger-pointing" have been developed. This includes both commercial solutions (e.g. Neurolucida 360; <http://www.mbfbioscience.com>) and freely available, academic software such as neuTube (<http://www.neutracing.com>; Feng et al., 2014) and hxskeletonize (developed for the Amira environment, Evers et al., 2005; Evers and Duch, 2014). While there are substantial differences in the functionality and user interface, we have so far had limited success with such procedures with respect to morphological reconstructions of AII amacrine cells. A specific disadvantage of commercial software is that the code is not available for users to modify and improve for specific applications.

4.4. Performance evaluation

To evaluate the performance of our method, we compared the automatic and manual reconstructions using both volume projection overlap, tree structure similarity, and branch statistics. The metric developed for the DIADEM challenge (Brown et al., 2011; Gillette et al., 2011a) compares the dendritic topology of two reconstructions, together with the locations of terminations and bifurcations. Compared to other relevant studies (e.g. Gillette et al., 2011a), we obtained very high DIADEM metric scores when comparing automatic and manual reconstructions, but it is not straightforward to compare the numerical values of such scores for reconstructions of different types of neurons. Unfortunately, we have no direct comparison for AII amacrine cells. Importantly, however, we inspected the results of the DIADEM algorithm, i.e., which nodes were marked as missed and spurious, and selected parameter settings that gave the most accurate assessment of the reconstruction quality. This resulted in a score of 0.950 ± 0.019 , similar to a score of 0.943 ± 0.026 for a similar data set of AII cells for which the reconstructions of two human operators were compared (unpublished observations). Our algorithm scored very well and in general produced excellent reconstructions of the tree structure. Most points were lost for discrepancies in the

existence and length of small dendritic tips (Fig. 5, 7, 9), although this is arguably in part due to a limited accuracy of the gold standard (e.g. Fig. 5D). This is also reflected in the average score of 0.87 for the DIADEM olfactory projection fiber data set we reconstructed, which requires a high spatial accuracy to correctly match nodes and contains a relatively large number of endings. Our score is comparable to scores obtained with other algorithms for the same dataset (0.80 - 0.95; Chothani et al., 2011; Türetken et al., 2011; Zhao et al., 2011).

In addition to the DIADEM metric, we applied the Dice coefficient to evaluate the projection overlap. An advantage of the Dice coefficient compared to the DIADEM metric is that it (indirectly) also evaluates the dendrite diameters. Similarity indices like the Dice coefficient are applied extensively to evaluate segmentation results for various objects and organs in medical images. Misiak et al. (2014) applied such indices to 2D acquisitions of neurons (under the name F-score) with reported scores between 0.56 and 0.81 for the methods evaluated in their study. Compared to these results, our method performed very well, but we have no direct comparison for AII amacrine cells of our method with other methods. A clear disadvantage of the Dice coefficient is that it ignores the actual branching structure and therefore primarily scores the quality of the initial segmentation.

Finally, we compared the automatic and manual reconstructions by analyzing the branch statistics, including Sholl analysis and distribution of branch length and diameter. Despite a high degree of similarity between the two methods, the most important differences were that the automatic reconstructions generated a number of spurious, short terminal branches and thicker branch diameters. Together, these differences resulted in a larger surface area of ~45% compared to the manual reconstructions. Potentially, the parameters of the automatic reconstruction algorithm could be adjusted to generate smaller branch diameters to more closely match the manual reconstructions.

4.5. Future developments

We can identify two reasons for attempting to reduce the computation time required for automatic reconstruction. For off-line reconstruction, reduced time is always favourable and will in general increase throughput and productivity. In addition, however, there is strong interest in being able to perform fast and accurate automatic morphological reconstruction on-line during an experiment, essentially in parallel with electrophysiological recording (Losavio et al., 2008). This approach has the potential to provide feedback to and guide experimental design within the duration of a single experiment, potentially boosting the results from combined structural-functional studies, and close to real-time reconstruction would be a great advancement. For the procedure used in the current study, it is likely that faster automated reconstruction can be achieved with a re-implementation in C++ or the recently developed Julia high-performance programming language (<http://julialang.org>). An implementation on a graphics processing unit (GPU), similar to that recently introduced for real-time deconvolution (e.g. the HyVolution system) could further decrease the processing time.

Information sharing statement

Code in the TREES toolbox (see Cuntz et al., 2010, 2011) and CellSegm toolbox (see Hodneland et al., 2013) is already publicly available. All additional code developed for the current project will be made available in open source (https://www.researchgate.net/profile/Bas-Jan_Zandt).

Acknowledgement

We thank John Georg Riisdal for contributions to an initial stage of the project. This work was supported by The Research Council of Norway (grants NFR 182743, 189662, 214216 to E.H.; NFR 213776 to M.L.V.), the Faculty of Medicine and Dentistry at the University of Bergen (fellowship for A. Losnegård), and the Meltzer fund (University of Bergen). The funders had no role in study design, data collection and interpretation,

or the decision to submit the work for publication. We thank Torhild Fjordheim Sunde for excellent technical assistance.

References

Acciai L, Soda P, Iannello G. Automated neuron tracing methods: an updated account. Neuroinform 2016; doi:10.1007/s12021-016-9310-0, epub ahead of print.

Ascoli GA, Svoboda K, Liu Y. The DIADEM Challenge. <http://diademchallenge.org/>; 2009-2010.

Basu S, Condron B, Aksel A, Acton S. Segmentation and tracing of single neurons from 3D confocal microscope images. IEEE J Biomed Health Inform 2013;17:319-335.

Brown KM, Barrientos G, Carty AJ, De Paola V, Hirsch JA, Jefferis GSXE, Lu J, Snippe M, Sugihara I, Ascoli GA. The DIADEM data sets: representative light microscopy images of neuronal morphology to advance automation of digital reconstructions. Neuroinform 2011;9:143-157.

Cannon RC, Turner DA, Pyapali GK, Wheal HV. An on-line archive of reconstructed hippocampal neurons. J Neurosci Meth 1998;84:49-54.

Capowski JJ. Computer Techniques in Neuroanatomy. New York: Plenum Press; 1989.

Cembrowski MS, Logan SM, Tian M, Jia L, Li W, Kath WL, Riecke H, Singer JH. The mechanism of repetitive spike generation in an axonless retinal interneuron. Cell Rep 2012;1:155-166.

Chothani P, Mehta V, Stepanyants A. Automated tracing of neurites from light microscopy stacks of images. Neuroinform 2011;9:263-278.

Cuntz H, Forstner F, Borst A, Häusser M. One rule to grow them all: a general theory of neuronal branching and its practical application. PLoS Comput Biol 2010;6:1-14.

Cuntz H, Forstner F, Borst A, Häusser M. The TREES toolbox – probing the basis of axonal and dendritic branching. *Neuroinform* 2011;9:91-96.

Cuntz H, Remme MWH, Torben-Nielsen B, editirs. The Computing Dendrite. From Structure to Function. Springer Series in Computational Neuroscience, vol. 11. Series editors. Destexhe A, Brette R. New York: Springer; 2014.

Dice LR. Measures of the amount of ecologic association between species. *Ecology* 1945;26:297-302.

Dodt HU, Frick A, Kampe K, Ziegglänsberger W. NMDA and AMPA receptors on neocortical neurons are differentially distributed. *Eur J Neurosci* 1998;10:3351-3357.

Donohue DE, Ascoli GA. Automated reconstruction of neuronal morphology: an overview. *Brain Res Rev* 2011;67:94-102.

Evers JF, Duch C. Quantitative geometric three-dimensional reconstruction of neuronal architecture and mapping of labeled proteins from confocal image stacks. In: Bakota L, Brandt R, editors. *Laser Scanning Microscopy and Quantitative Image Analysis of Neuronal Tissue*. Berlin, New York: Springer; 2014. p. 219-237.

Evers JF, Schmitt S, Sibila M, Duch C. Progress in functional neuroanatomy: precise automatic geometric reconstruction of neuronal morphology from confocal image stacks. *J Neurophysiol* 2005;93:2331-2342.

Feng L, Zhao T, Kim J. neuTube 1.0: A new design for efficient neuron reconstruction software based on the SWC format. *eNeuro* 2014; DOI: 10.1523/ENEURO.0049-14.

Gillette TA, Brown KM, Ascoli GA. The DIADEM metric: comparing multiple reconstructions of the same neuron. *Neuroinform* 2011a;9:233-245.

Gillette TA, Brown KM, Svoboda K, Liu Y, Ascoli GA. DIADEMchallenge.Org: a compendium of resources fostering the continuous development of automated neuronal reconstruction. *Neuroinform* 2011b;DOI 10.1007/s12021-011-9104-3.

Glaser JR, Glaser EM. Neuron imaging with Neurolucida - a PC-based system for image combining microscopy. *Comput Med Imaging Graph* 1990;14:307-317.

Hartveit E. Membrane currents evoked by ionotropic glutamate receptor agonists in rod bipolar cells in the rat retinal slice preparation. *J Neurophysiol* 1996;76:401-422.

Hartveit E, Veruki ML. Electrical synapses between AII amacrine cells in the retina: Function and modulation. *Brain Res* 2012;1487:160-172.

Hodneland E, Kögel T, Frei DM, Gerdes HH, Lundervold A. CellSegm - a MATLAB toolbox for high-throughput 3D cell segmentation. *Source Code Biol Med* 2013;8:16.

Jacobs G, Claiborne B, Harris K. Reconstruction of neuronal morphology. In: De Schutter E, editor. Computational Modeling Methods for Neuroscientists. Cambridge: MIT Press; 2010. p. 187-210.

Jaeger D. Accurate reconstruction of neuronal morphology. In: De Schutter E, editor. Computational Neuroscience: Realistic Modeling for Experimentalists. Boca Raton: CRC Press; 2001. p. 159-178.

Jefferis GS, Potter CJ, Chan AM, Marin EC, Rohlfing T, Maurer CR Jr, Luo L. Comprehensive maps of Drosophila higher olfactory centers: spatially segregated fruit and pheromone representation. *Cell* 2007;128:1187-1203.

Kroon DJ. Accurate Fast Marching toolbox for MATLAB.
[www.mathworks.com/matlabcentral/fileexchange/ 24531-accurate-fast-marching](http://www.mathworks.com/matlabcentral/fileexchange/24531-accurate-fast-marching).
2009.

Lee T-C, Kashyap RL, Chu C-N. Building skeleton models via 3-D medial surface / axis thinning algorithms. *CVGIP: Graph Models Image Process* 1994;56:462-478.

Losavio BE, Liang Y, Santamaría-Pang A, Kakadiaris IA, Colbert CM, Saggau P. Live neuron morphology automatically reconstructed from multiphoton and confocal imaging data. *J Neurophysiol* 2008;100:2422-2429.

Maurer CR, Qi R, Raghavan V. A linear time algorithm for computing exact Euclidean distance transforms of binary images in arbitrary dimensions. *IEEE Trans Pattern Analysis and Machine Intelligence* 2003;25:265-270.

Meijering E. Neuron tracing in perspective. *Cytometry A* 2010;77:693-704.

Mishchenko Y. A fast algorithm for computation of discrete Euclidean distance transform in three or more dimensions on vector processing architectures. *Signal, Image and Video Processing* 2015;9:19-27.

Misiak D, Posch S, Lederer M, Reinke C, Hüttelmaier S, Müller B. Extraction of protein profiles from primary neurons using active contour models and wavelets. *J Neurosci Meth* 2014;225:1-12.

Murphy DB, Davidson MW. Fundamentals of Light Microscopy and Electronic Imaging. 2013, 2nd ed. Hoboken: Wiley-Blackwell.

Myatt DR, Hadlington T, Ascoli GA, Nasuto SJ. Neuromantic - from semi-manual to semi-automatic reconstruction of neuron morphology. *Front Neuroinform* 2012;6:4.

Nörenberg A, Hu H, Vida I, Bartos M, Jonas P. Distinct nonuniform cable properties optimize rapid and efficient activation of fast-spiking GABAergic interneurons. *Proc Natl Acad Sci USA* 2010;107:894-899.

Pagliaroni DW. Distance transforms: properties and machine vision applications. *CVGIP: Graph Models Image Process* 1992;54:56-74.

Parekh R, Ascoli GA. Neuronal morphology goes digital: a research hub for cellular and system neuroscience. *Neuron* 2013;77:1017-1038.

Peng H, Long F, Myers G. Automatic 3D neuron tracing using all-path pruning. *Bioinformatics* 2011a;27:i239-i247.

Peng H, Long F, Zhao T, Myers G. Proof-editing is the bottleneck of 3D neuron reconstruction: the problem and solutions. *Neuroinform* 2011b;9:103-105.

Peng H, Meijering E, Ascoli GA. From DIADEM to BigNeuron. *Neuroinform* 2015;13:259-260.

Peng H, Ruan Z, Long F, Simpson JH, Myers EW. V3D enables real-time 3D visualization and quantitative analysis of large-scale biological image data sets. *Nat Biotech* 2010;28:348-353.

Pologruto TA, Sabatini BL, Svoboda K. Scanimate: flexible software for operating laser scanning microscopes. *Biomed Eng Online* 2003;2:13.

Prim RC. Shortest connection networks and some generalizations. *Bell Syst Technol J* 1957;36:1389-1401.

Ramón y Cajal S. *Histologie du Système Nerveux de l'Homme et des Vertébrés*. 1909, Vol. I. Maloine, Paris, France.

Ramón y Cajal S. *Histologie du Système Nerveux de l'Homme et des Vertébrés*. 1911, Vol. II. Maloine, Paris, France.

Rodriguez A, Ehlenberger DB, Hof PR, Wearne SL. Three-dimensional neuron tracing by voxel scooping. *J Neurosci Meth* 2009;184:169-175.

Santamaría-Pang A, Colbert CM, Losavio B, Saggau P, Kakadiaris IA. Automatic morphological reconstruction of neurons from optical imaging. In: Proc. of the International Workshop in Microscopic Image Analysis and Applications in Biology (MIAAB), Piscataway, NJ, Sept 21, 2007.

Santamaría-Pang A, Hernandez-Herrera P, Papadakis M, Saggau P, Kakadiaris IA. Automatic morphological reconstruction of neurons from multiphoton and confocal microscopy images using 3D tubular models. *Neuroinform* 2015;13:297-320.

Schindelin J, Arganda-Carreras I, Frise E, Kaynig V, Longair M, Pietzsch T, Preibisch S, Rueden C, Saalfeld S, Schmid B, Tinevez JY, White DJ, Hartenstein V, Eliceiri K, Tomancak P, Cardona A. Fiji: an open-source platform for biological-image analysis. *Nat Methods* 2012;9:676-682.

Schneider CJ, Cuntz H, Soltesz I. Linking macroscopic with microscopic neuroanatomy using synthetic neuronal populations. PLoS Comput Biol 2014;10:e1003921

Sethian JA. A fast marching level set method for monotonically advancing fronts. Proc Natl Acad Sci USA 1996;93:1591-1595.

Sholl DA. Dendritic organization in the neurons of the visual and motor cortices of the cat. J Anat 1953;87: 387-406.

Türetken E, González G, Blum C, Fua P. Automated reconstruction of dendritic and axonal trees by global optimization with geometric priors. Neuroinform 2011;9:279-302.

Turner DA, Wheal HV, Stockley E, Cole H. Three-dimensional reconstructions and analysis of the cable properties of neurons. In: Chad J, Wheal H, editors. Cellular Neurobiology. A Practical Approach. Oxford: IRL Press at Oxford University Press; 1991. p. 225-246.

van der Voort HTM, Strasters KC. Restoration of confocal images for quantitative image analysis. J Microscopy 1995;178:165-181.

Weickert J. A review of nonlinear diffusion filtering. In: ter Haar Romeny B, Florack L, Koenderink J, Viergever M, editors. Scale-Space Theory in Computer Vision. Lecture Notes in Computer Science, Vol. 1252. Berlin: Springer; 1997. p. 3-28.

Wu C, Ivanova E, Cui J, Lu Q, Pan Z-H. Action potential generation at an axon initial segment like process in the axonless retinal AII amacrine cell. J Neurosci 2011;31:14654-14659.

Xiao H, Peng H. APP2: automatic tracing of 3D neuron morphology based on hierarchical pruning of a gray-weighted image distance-tree. Bioinformatics 2013;29:1448-1454.

Zandt B-J, Liu JH, Veruki ML, Hartveit E. AII amacrine cells: quantitative reconstruction and morphometric analysis of electrophysiologically identified cells in live rat retinal slices imaged with multi-photon excitation microscopy. Brain Struct Funct 2016; DOI: 10.1007/s00429-016-1206-0.

Zhao T, Xie J, Amat F, Clack N, Ahammad P, Peng H, Long F, Myers E. Automated reconstruction of neuronal morphology based on local geometrical and global structural models. Neuroinform 2011;9:247-261.

Figure Legends

Fig. 1. Overview of the algorithm and work flow for automatic reconstruction of neuronal morphology. Each box summarizes a series of steps that together constitute a processing stage, the name of which is indicated at the upper left corner of each box. The user is prompted for input twice during the procedure (indicated by "user input" in the work flow). Abbreviations: maximum intensity projection (MIP); three dimensional (3D); minimum spanning tree (MST).

Fig. 2. Workflow for multiphoton excitation microscopic imaging and preprocessing during morphological reconstruction of dye-filled AII amacrine cells. (A) Maximum intensity projection of raw image stack of cell filled with Alexa 594 during whole cell recording (dye-filled pipette attached to the cell body). (B) Same as in (A), but after deconvolution and alignment. Areas with increased background fluorescence caused by leakage of fluorescent dye are circumscribed by dashed lines. (C) Same as in B, but after removal of fluorescence corresponding to pipette and contaminating areas. Continuous line corresponds to manually delineated region containing the cell, outside of which fluorescence was removed. To enhance visibility, contrast in all panels was increased by 50%, leading to saturation of areas with higher intensity. Scale bar 10 μm (A-C).

Fig. 3. Workflow of segmentation of an image stack containing an isolated neuron. (A) Result of the initial intensity segmentation of an image stack containing an AII amacrine cell (cf. section 2.7). The different parts of the cell are displayed as a surface rendering, with the main part in gray and the various disconnected segments in a series of different colors. (B, C) For each disconnected segment, the path of the Fastest March towards the soma was calculated (cf. sections 2.8 and 2.9). The paths (red) are displayed together with a cell surface rendering (gray), both semi-transparent (B) and non-transparent (C) for enhanced visualization. (D) The thresholded cell volume merged with the Fast Marching paths. The originally disconnected segments and the paths

form a single connected volume that is subsequently used for skeletonization. Notice that to simplify the display of the extensively branching dendritic trees, we selected a cell with relatively few branches. Scale bar 10 μm (A-D).

Fig. 4. Workflow for skeletonization and tubularization of the segmented image stack. For each step, the result is displayed both in frontal (XY) view (along the Z axis according to the spatial coordinates defined during multiphoton excitation microscopic imaging; *top row*) and in side (YZ) view (along the X axis; *bottom row*). (A) Isosurface renderings of the segmented stack. Note that the cell appears much thicker in side view (*bottom*) than in frontal view (*top*) due to the lower axial than lateral resolution of light microscopy. (B) Result after skeletonization of the segmented volume. Shaded areas (light gray) correspond to the user-selected soma region used for branch removal. Here, and in (C), the skeleton appears thicker in the side view (*bottom*) due to the anisotropic voxel dimensions, being larger in the Z- than in the XY-direction. (C) Skeleton after removal of the spurious branches created inside and around the soma. (D) Tree structure generated from the skeleton, rendered as cylindrical segments. For each reconstruction point, the dendritic diameter was determined as that of the largest sphere fitting inside the segmented volume. Scale bar 10 μm (A-D).

Fig. 5. Results of tubularization and comparison with automatic and manual segmentations. (A-D) The segmented and tubularized volumes are projected in 2D and the outlines of these projections are overlaid on a maximum intensity projection of the image stack. The results for the same part of the image stack are displayed both in frontal (XY) view (A, C) and in side (YZ) view (B, D). (A, B) Comparison of the results of tubularization (*yellow*) with the results from the automatic segmentation (*red*). (C, D) Comparison of the results of tubularization (*yellow*) with the results from the manual segmentation (*red*). Notice that the tubular format adequately describes the shape of the dendrites and appears approximately equal to the segmented volume in the front view, for both automatic and manual segmentation (A, C). For the automatic

segmentation, the tubularization compensates for the elongated appearance of the segmented volume in the Z-direction (B). The result of the tubularization corresponds well with that of the manual segmentation also in the Z-direction (D). Notice that with the projection of the outlines of the segmented stacks in 2D, crossing of branches gives rise to a false impression of the presence of loops and holes (A-D). Scale bar 2 μm (A-D).

Fig. 6. Procedure for generating the soma contour. (A) Contour of the segment containing the soma (white line) in a slice of the segmented image stack displayed together with initial location of center point inside the soma (white cross). An example radius (r ; indicated by white arrow) with angle θ originates from the center point. (B) Contour in (A) represented in polar coordinates, with the center point displayed in (A) as origin (solid line). Peaks are cut off using an order-statistic filter (*ordfilt2* function in MATLAB) (dashed line). (C) Resulting contour and corrected center point (after 10 iterations), same slice as in (A). (D) Cross-sectional area of contour in each slice of the image stack as function of depth in the stack (open circles; top slice in stack located at a depth of 0 μm). Data points have been fitted with a smoothing function (2nd order Savitzky-Golay filter with window length of 8 μm ; continuous line). The contour in the slice corresponding to the peak of the cross-sectional area is selected to represent the soma contour. Scale bar 5 μm (A, C).

Fig. 7. Comparison of tree structures generated by automatic and manual segmentation of an AII amacrine cell. (A) Result from automatic segmentation. (B) Result from manual segmentation. (C) Overlay of tree structures generated by automatic and manual segmentation (*blue*, automatic; *red*, manual). (A-C) Spurious and missed nodes are marked with x/X and o/O , respectively. Small markers (x, o) denote mismatches of branch endings, large markers (X, O) denote mismatches of (centripetally) higher-order branch points. The tree structure itself contains relatively few errors and most errors correspond to spurious and missed branch endings. Notice

the very high degree of similarity between the automatic and the manual tree structures. Scale bar 10 μm (A-C).

Fig. 8. Comparison of the isosurfaces generated by automatic and manual segmentation of an AII amacrine cell. (A) Isosurface from automatic segmentation (*blue*) and automatically generated soma contour (*black, top*). (B) Isosurface from manual segmentation (*red*) and manually generated soma contour (*black, top*). (C) Overlay of projections of the segmentations generated by automatic and manual segmentation (*blue*, automatic; *red*, manual; *gold*, overlap). For each case (A-C), the result is displayed both in frontal (XY) view (along the Z axis; *top row*) and in side (YZ) view (along the X axis; *bottom row*).

Fig. 9. Qualitative comparison of reconstruction results for different regions of the dendritic tree of an AII amacrine cell. (A) Maximum intensity projection (MIP) of preprocessed image stack (white). Four different regions are indicated by red boxes and are displayed at higher magnification in (B-E). (B-E) Magnified display of the corresponding regions in (A), each row (from *left* to *right*) shows results from the automatic (*blue*) and manual (*red*) reconstructions rendered as a series of short cylinders overlaid on the MIP, overlaid projections of the reconstructed volumes (*blue*, automatic; *red*, manual; *gold*, overlap), and a schematic representation of the tree structure (*blue*, automatic; *red*, manual). Arrows point to differences between the automated and manual reconstructions (see Results). Scale bar, 10 μm .

Fig. 10. Analysis of branch statistics of automatically (continuous lines) and manually (dashed lines) reconstructed AII amacrine cells ($n = 10$). (A) Average frequency distribution of branch segment path lengths. Bin width 1 μm (A - C). (B) As in (A), but after removing all short ($< 1 \mu\text{m}$) terminal branches to allow for a better comparison of the distribution of branch segment lengths of the main structure of the reconstructions. (C) Sholl analysis of process length as a function of Euclidean distance from the center

of the cell body. (D) Average distribution of process diameters. Bin width 0.1 μm . Notice that "branch segment" is defined as the part of a branch between two nodes or between a node and a termination point. This follows the terminology of Capowski (1989), adopted by e.g. Zandt et al. (2016) and the Neurolucida software, but differs from that used by the TREES toolbox.

Fig. 11. Qualitative comparison of reconstruction results for an olfactory projection fiber from the DIADEM data set. (A-C) Results from the automatic (*blue*) and manual (*red*) reconstructions rendered as a series of short cylinders overlaid on MIPs of the image stack. For clarity, the automatic and manual reconstructions have been shifted relative to each other. The region indicated by the white box (A) is displayed at higher magnification in (B, C). (B, C) Magnified display of the corresponding region in (A). Arrows point to some branches missed or reconstructed too short by the automatic reconstruction (B, C, E). (D) Schematic representation of the tree structure (*blue*, automatic; *red*, manual), symbols indicate missed (o) and spurious (x) branches as obtained by the DIADEM algorithm (D, E). (E) Magnified display of the corresponding boxed region in (D). Arrows as in (B, C). Scale bars, 10 μm (A), (B, C, E), (D).

Table 1

DIADEM metric scores and Dice coefficients, obtained by comparing our method for automatic reconstruction with manual reconstruction.

Cell	DIADEM metric	Dice coefficient
1	0.972	0.867
2	0.955	0.875
3	0.969	0.864
4	0.972	0.854
5	0.946	0.866
6	0.920	0.863
7	0.930	0.853
8	0.958	0.856
9	0.949	0.826
10	0.928	0.847
Mean \pm SD	0.950 ± 0.019	0.857 ± 0.014

The parameters for DIADEM metric scores were set to $x = 3 \mu\text{m}$, $z = 3 \mu\text{m}$, $xy\text{PathThresh} = 0.2$ and $z\text{PathThresh} = 0.2$. Both scores have values in the interval $[0, 1]$ and higher scores indicate better match. Last row denotes mean values and standard deviations across the sample.

Table 2

Comparison of branching properties between manual and automatic reconstructions of AII amacrine cells ($n = 10$).

Parameter	Manual (Mean ± SD)	Automatic (Mean ± SD)	Ratio (Mean ± SD)
Number of nodes	195 ± 56	298 ± 92	1.55 ± 0.30
Number of endings	207 ± 59	308 ± 97	1.51 ± 0.28
Dendritic length	1110 ± 270	1290 ± 380	1.15 ± 0.13
Average dendritic diameter (μm)	0.488 ± 0.044	0.612 ± 0.051	1.27 ± 0.19
Dendritic surface area (μm ²)	1690 ± 380	2490 ± 760	1.45 ± 0.17

Metrics were obtained from the TREES toolbox (v 1.15; Cuntz et al., 2010, 2011) and terminology follows that used by Zandt et al. (2016).

Ratio: obtained by dividing the result obtained with automatic reconstruction by that obtained with manual reconstruction.

Average dendritic diameter: obtained by averaging the diameters for the branch sections weighted by their lengths.

Table 2

Comparison of branching properties between manual and automatic reconstructions of AII amacrine cells ($n = 10$).

Parameter	Manual (Mean ± SD)	Automatic (Mean ± SD)	Ratio (Mean ± SD)
Number of nodes	195 ± 56	298 ± 92	1.55 ± 0.30
Number of endings	207 ± 59	308 ± 97	1.51 ± 0.28
Dendritic length	1110 ± 270	1290 ± 380	1.15 ± 0.13
Average dendritic diameter (μm)	0.488 ± 0.044	0.612 ± 0.051	1.27 ± 0.19
Dendritic surface area (μm ²)	1690 ± 380	2490 ± 760	1.45 ± 0.17

Metrics were obtained from the TREES toolbox (v 1.15; Cuntz et al., 2010, 2011) and terminology follows that used by Zandt et al. (2016).

Ratio: obtained by dividing the result obtained with automatic reconstruction by that obtained with manual reconstruction.

Average dendritic diameter: obtained by averaging the diameters for the branch sections weighted by their lengths.

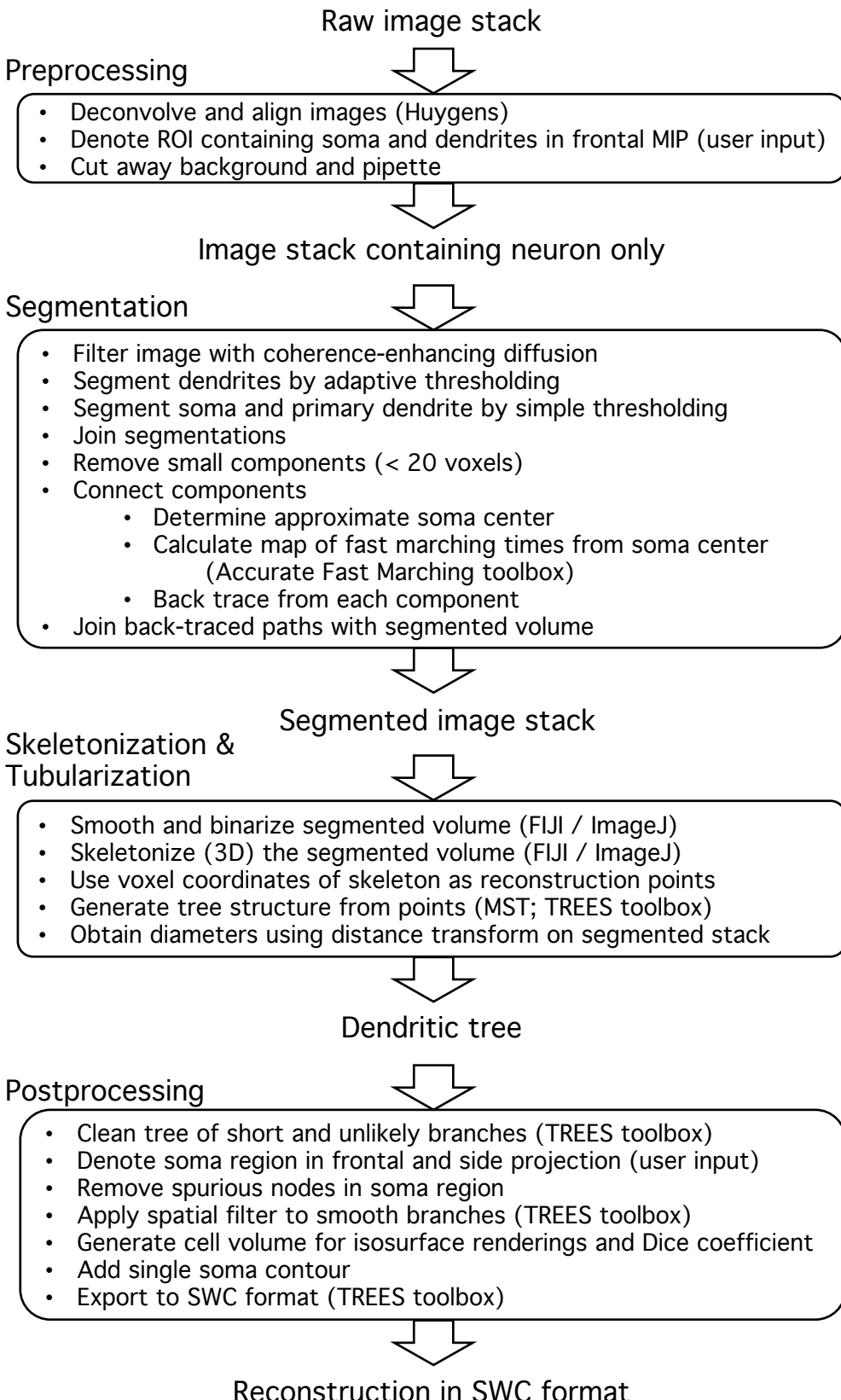


Figure 1 (Zandt et al.)

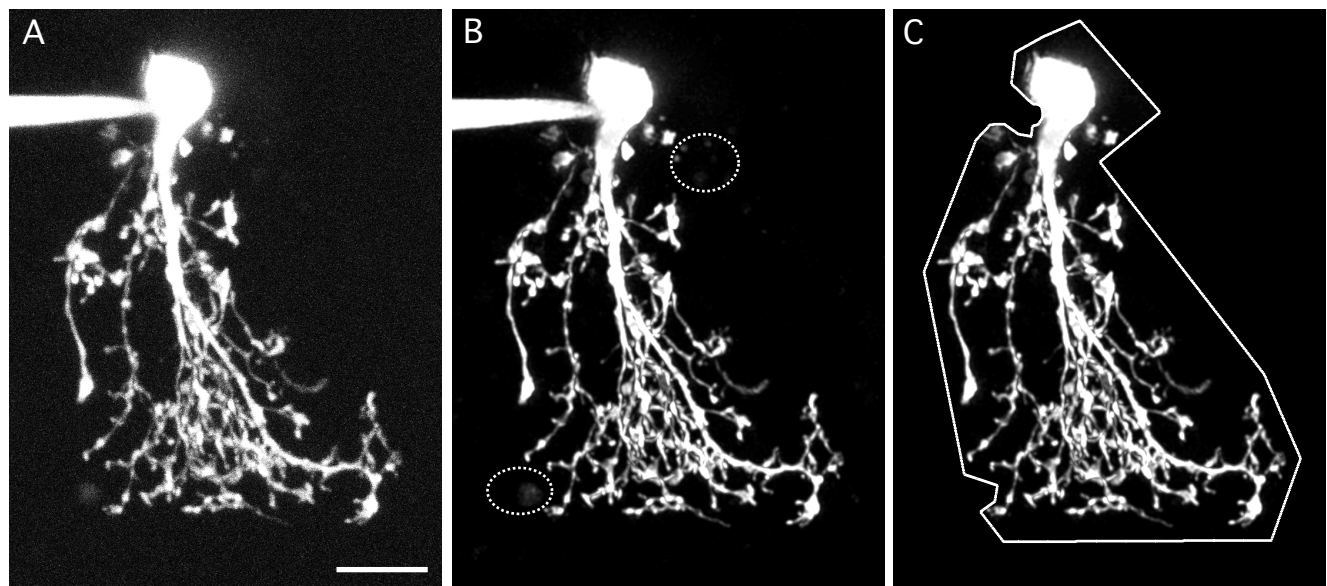


Figure 2 (Zandt et al.)

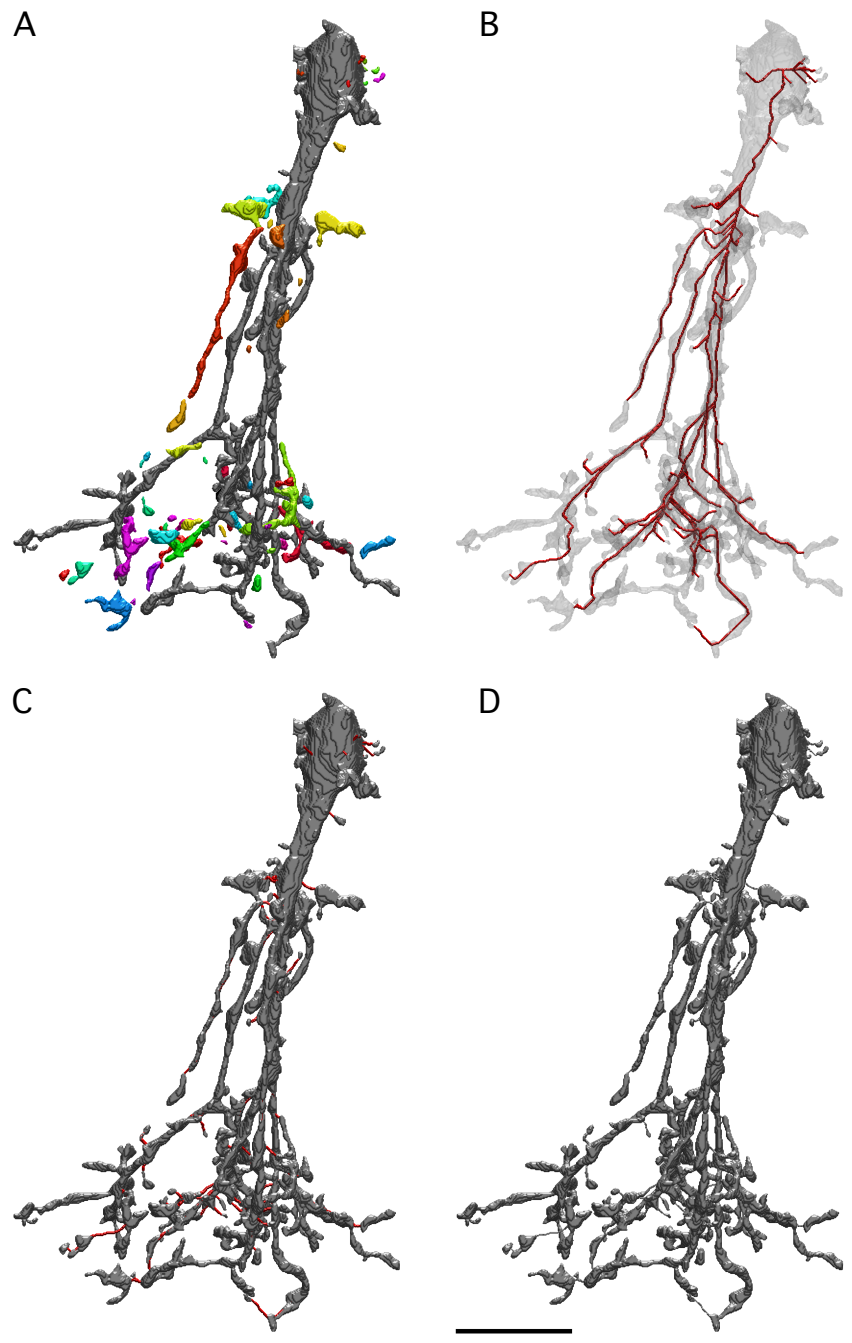


Figure 3 (Zandt et al.)

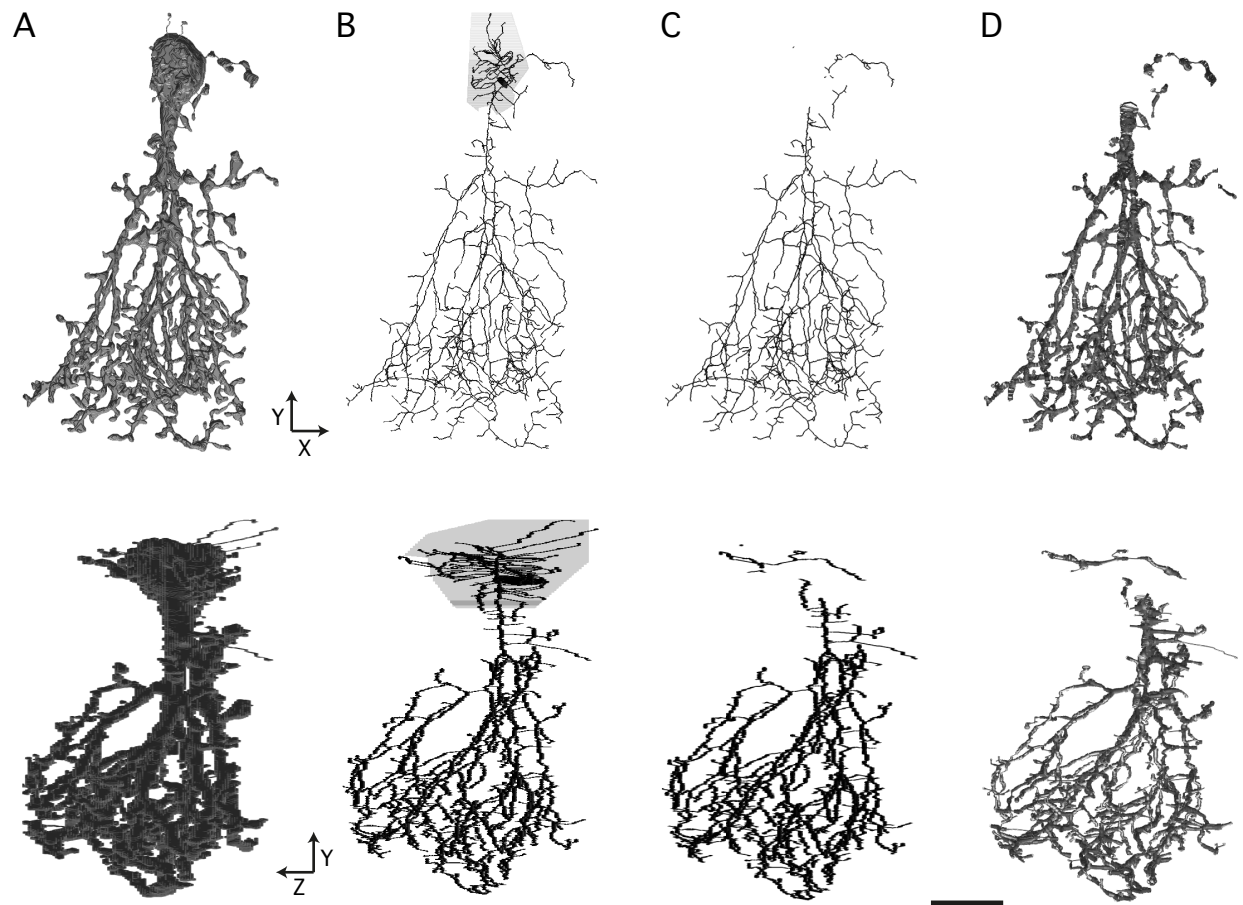


Figure 4 (Zandt et al.)

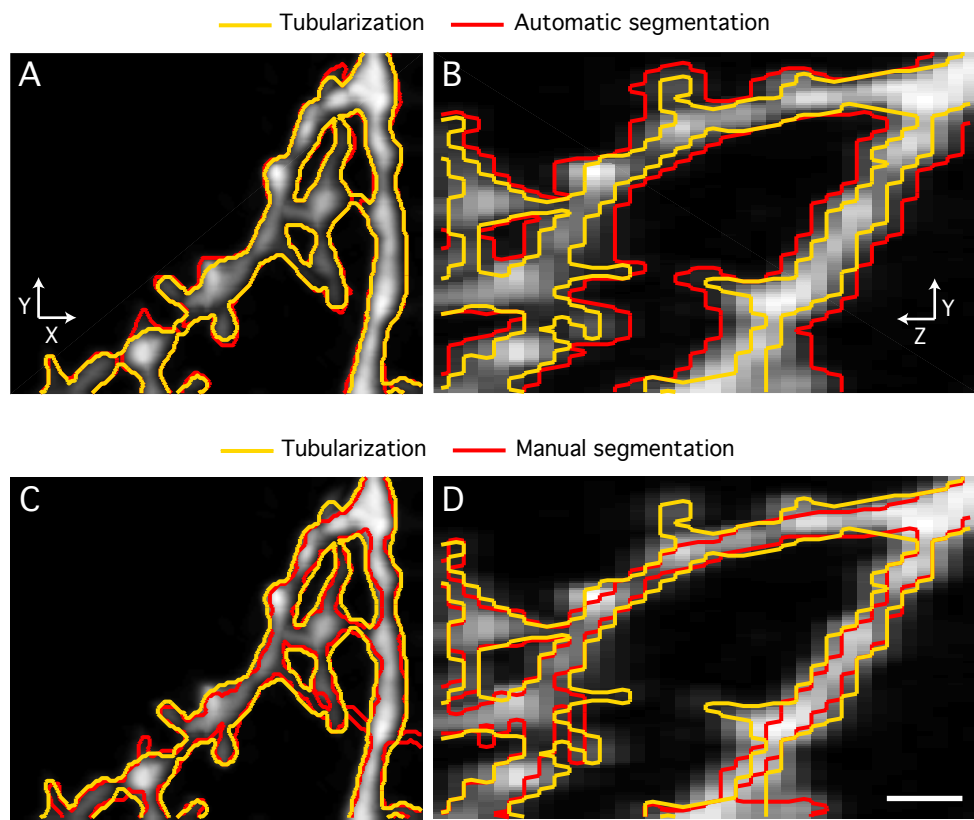


Figure 5 (Zandt et al.)

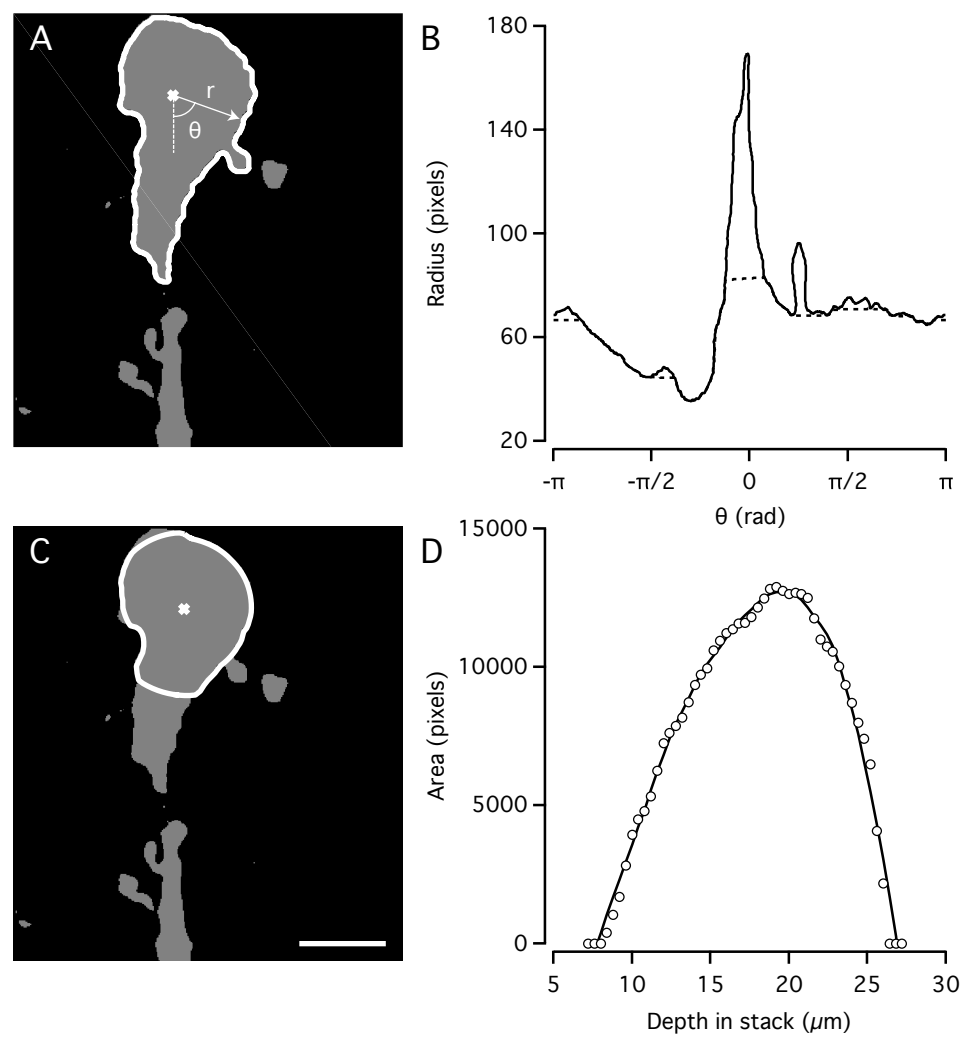


Figure 6 (Zandt et al.)

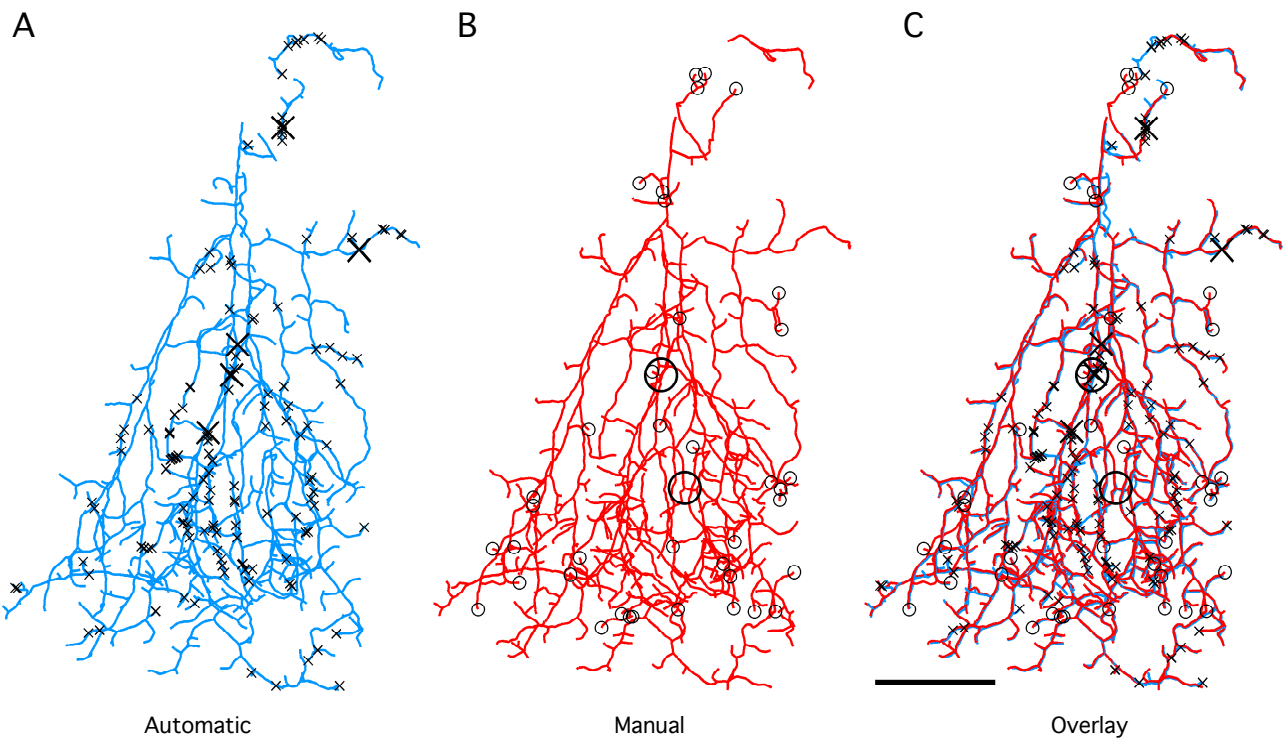


Figure 7 (Zandt et al.)

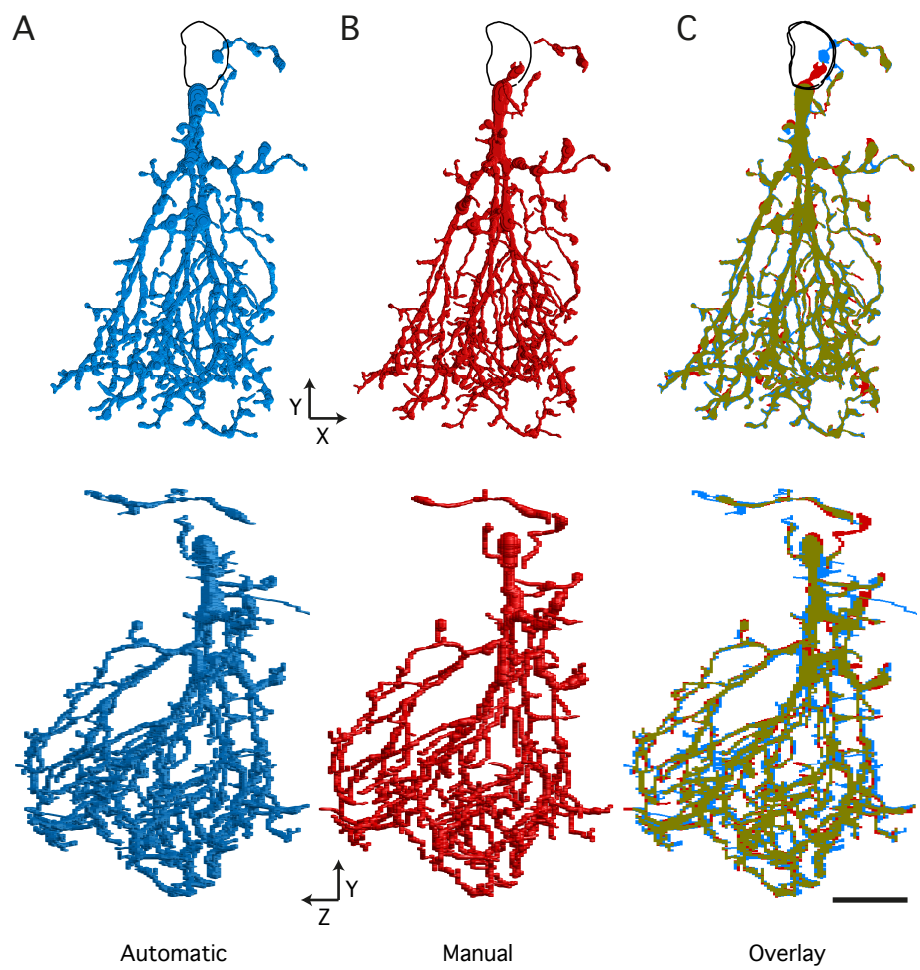


Figure 8 (Zandt et al.)

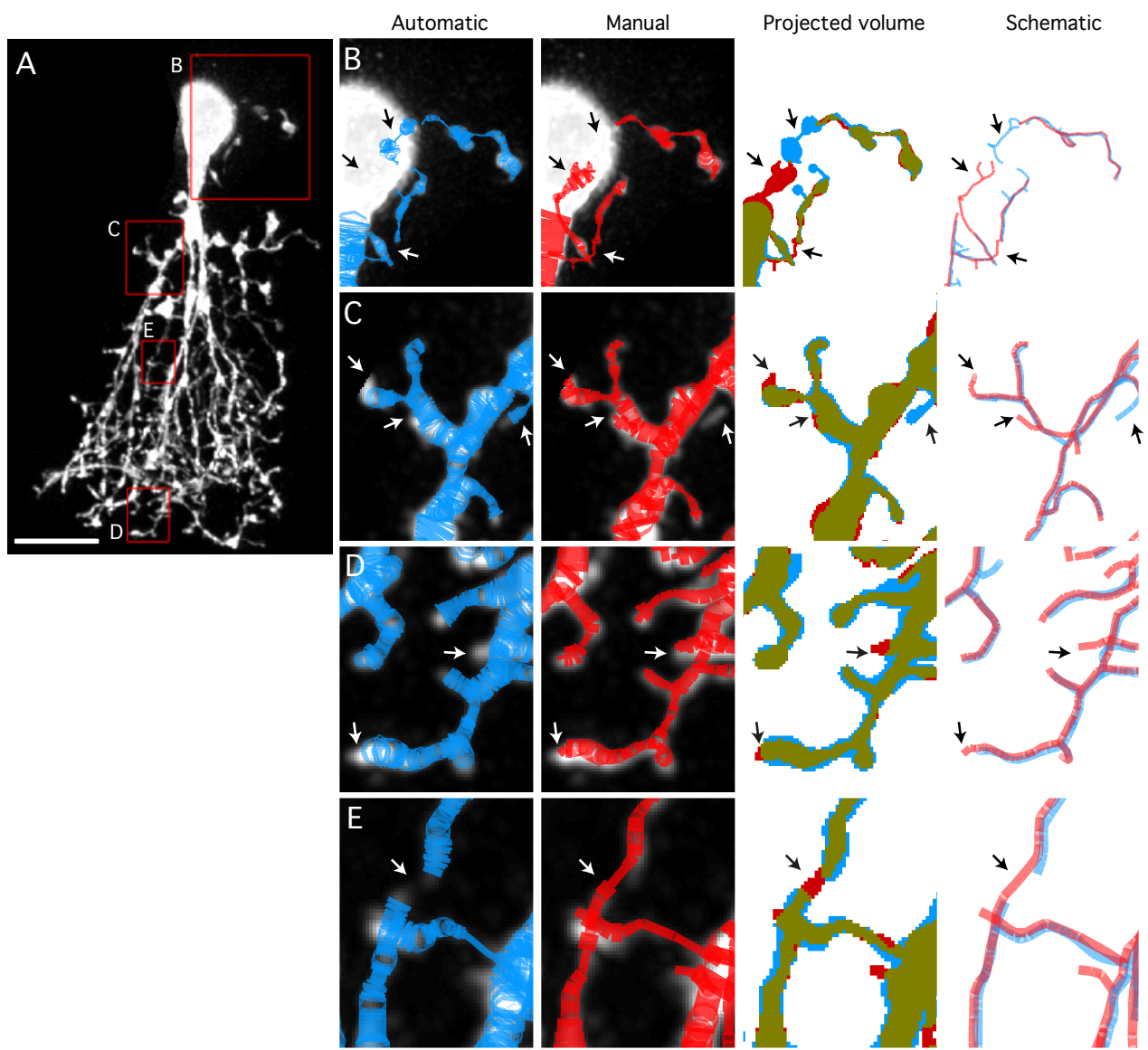


Figure 9 (Zandt et al.)

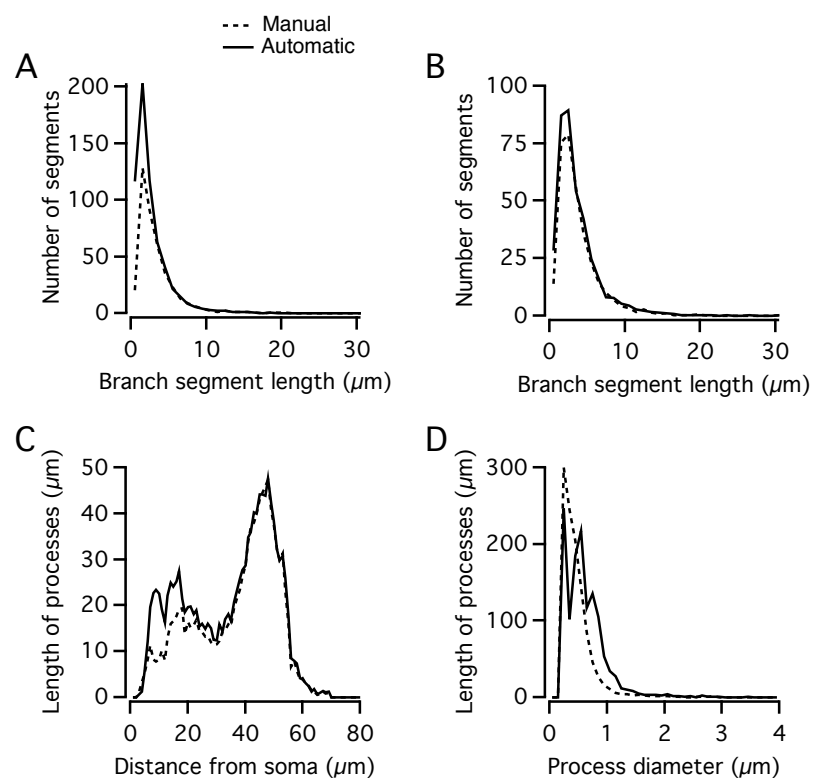


Figure 10 (Zandt et al.)

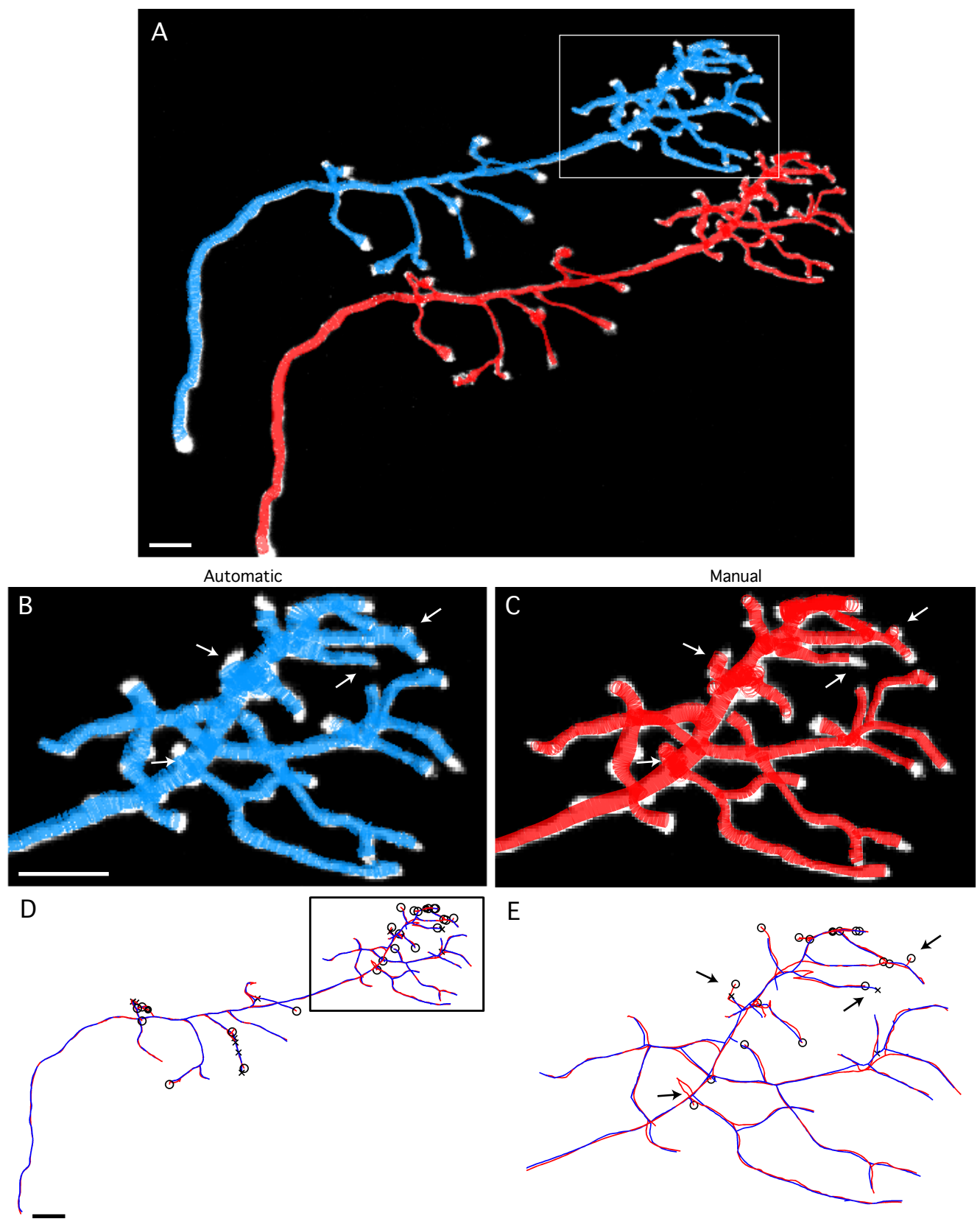


Figure 11 (Zandt et al.)